Electronic Supporting Information:

Supramolecular solvatochromism: mechanistic insight from crystallography, spectroscopy and theory

Varvara I. Nikolayenko,[a] Lisa M. van Wyk,[a] Orde Q. Munro[b*] and Leonard J. Barbour[a*]

[a] *Department of Chemistry and Polymer Science, University of Stellenbosch, 7602 Matieland, South Africa.* [b] *School of Chemistry, University of the Witwatersrand, PO WITS 2050, Johannesburg, South Africa.*

* Correspondence to Professors Leonard J. Barbour (Email: ljb@sun.ac.za) and Orde Q. Munro (Email: Orde.Munro@wits.ac.za).

Table of Contents

1. Ligand synthesis and crystallisation

All solvents and reagents were procured from reputable commercial distributors (Merck, Sigma-Aldrich) and were used without further purification.

1.1. Synthesis of ligand - 1,4-bis[(2-methylimidazol-1-yl)methyl]benzene

The ligand, 1,4-bis[(2-methylimidazol-1-yl)methyl]benzene, was synthesised via the synthetic route reported by Dobrzańska *et al.*[1] 2-methyl imidazole (0.82 g, 10 mmol) and potassium hydroxide (2.30 g, 41 mmol) were dissolved in dimethyl sulfoxide (15 ml). The reaction mixture was then stirred for approximately two hours. To the reaction mixture α-α'-dichloro-*p*-xylene (0.88 g, 5 mmol) was added and the reaction was left stirring overnight. A liquid-liquid extraction was carried out with dichloromethane (10 ml). After which the solution was dried over magnesium sulphate, filtered and reconcentrated. Excess diethyl ether was added and the flask placed in the refrigerator overnight to allow the product to precipitate out. The final product was a yellow powder obtained in a: 709.30 mg, 2.66 mmol, 26.6% yield.

δ_H (300 MHz, DMSO-d_6): δ (ppm) 2.20 (s, 6H), 5.11 (s, 4H), 6.75 (d, J = 1.17 Hz, 2H), 7.09 (d, J= 1.17 Hz, 2H), 7.12 (s, 4H).

MS (ESI^+) m/z 267 (25 %, $[M+H]^+$), 134 (100%, $[M+2H]^{2+}$)

Melting point: 79.7 – 81.7 °C

1.2. Crystallisation of 1

Bulk crystallisations were carried out by dissolving 1,4-bis[(2-methylimidazol-1-yl)methyl]benzene (47.3 mg, 0.178 mmol) in dimethyl sulfoxide (6 ml), and copper dichloride dihydrate (30.4 mg, 0.178 mmol) in ethanol (4 ml). The copper solution was then layered on the ligand solution. The resultant crystals were green and prismatic.

1.3. Guest exchange

Each guest exchange was performed by placing crystals of **1** in acetonitrile for 24 hours. Once the exchange was complete (this was monitored using PXRD and UV-visible spectroscopy) these crystals where immersed in either acetone, THF, diethyl ether or pentane. These exchanges were again monitored using UV and PXRD.

2. Single crystal X-ray diffraction (SCXRD)

Crystals of appropriate size possessing suitable morphology, transparency and ability to extinguish plane-polarised light were glued onto a glass fibre, where necessary, using epoxy or attached to the tip of a MiTeGen mount[2] using Paratone®N oil. X-ray intensity data was recorded on a Bruker SMART-APEX II, Bruker APEX II DUO or Bruker D8 Venture diffractometer. The SMART instrument is equipped with a molybdenum fine-focus sealed tube, a 0.5 mm Monocap collimator and an APEX II detector. The DUO instrument is equipped with Incoatec $I_{\mu}S$ molybdenum and copper microfocus X-ray sources and an APEX II detector. The Venture instrument is equipped with Incoatec $I_{\mu}S$ molybdenum microfocus X-ray sources and an APEX III detector. All diffractometers are fitted with an Oxford Cryosystems cryostat (700 Series Cryostream Plus for the SMART and DUO instruments and 800 Series Cryostream for the Venture instrument), which is used to control the sample temperature.

Data reduction and absorption corrections were carried out using the SAINT[3] and SADABS[4] programs, respectively. The unit cell dimensions were refined on all data and space groups were assigned based on systematic absences and intensity statistics. The structures were solved by direct methods or a combination of Patterson and partial structure expansion using SHELXS-97[5] and refined with SHELXL-97[4] using the X-Seed[6] graphical user interface. Non-hydrogen atoms were refined anisotropically. Hydrogen atoms were placed in calculated positions. Illustrations of all crystal structures were generated using the program POV-Ray.[7]

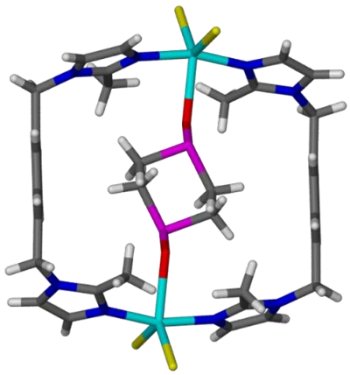

Figure S1: Capped-stick representation of **1**.

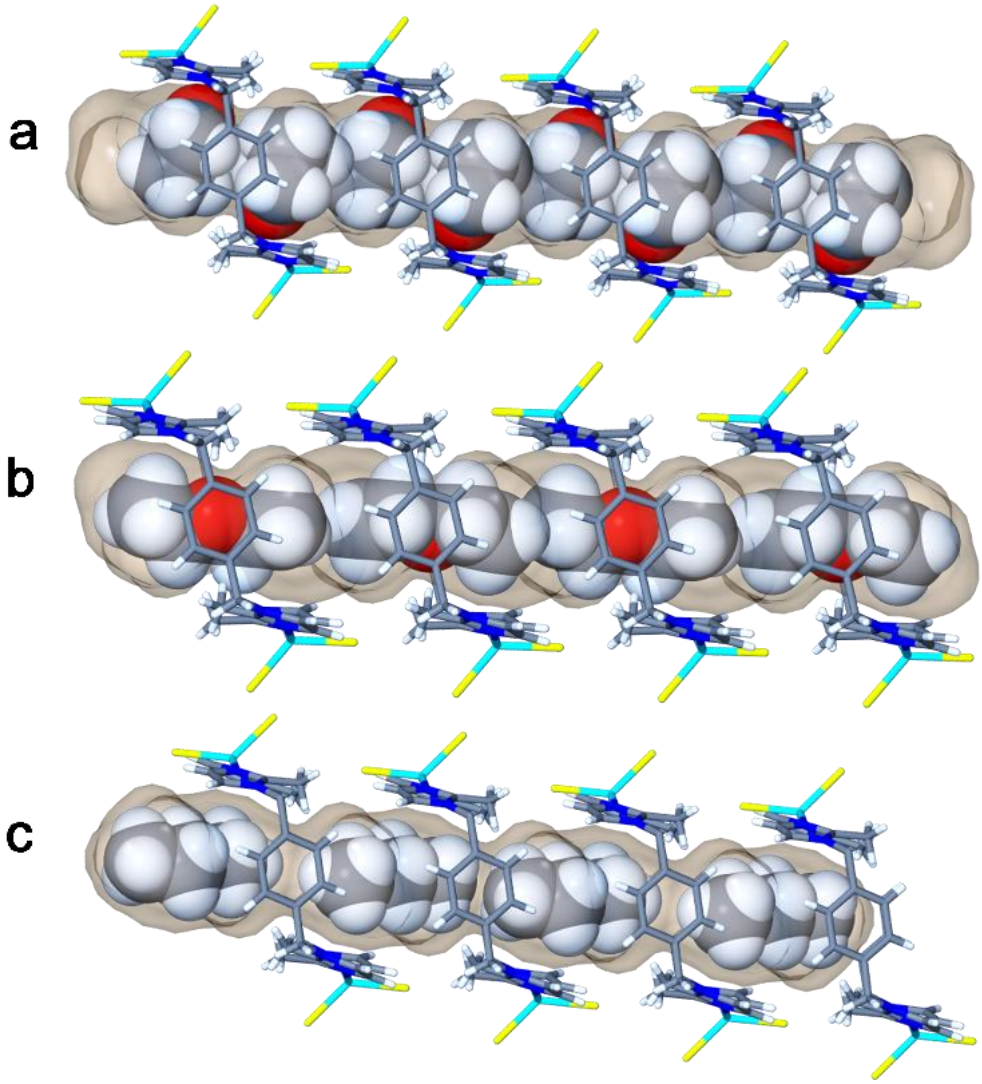

Figure S2: A perspective view of a column of metallocycles showing positions of (**a**) THF, (**b**) diethyl ether and (**c**) pentane in the solvent-accessible channels mapped in grey (probe radius 1.5 Å). In (**a**) two THF molecules are located in the space between metallocycles, with each oxygen heteroatom directed towards the copper centre of the nearest metallocycle. The single diethyl ether molecule in (**b**) is situated with the oxygen heteroatom in a central position within each metallocycle. The pentane molecule in (**c**) has no heteroatom and is thus positioned between two adjacent metallocycles.

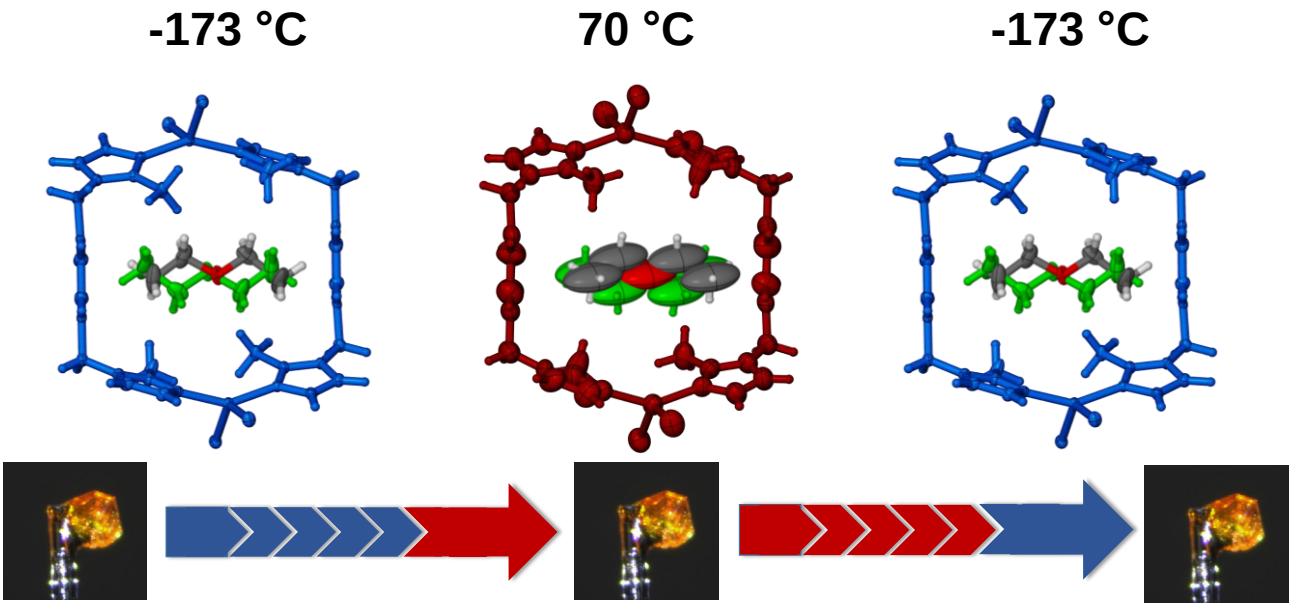

Figure S3: Crystal structure of **5** as it was cycled from –173 °C to 70 °C and back to –173 °C; images of the actual crystal used for the single-crystal to single-crystal transformation are shown

Table S1: Selected crystallographic parameters for the different solvates.

	1	2	3	4	5 (100 K)	5 (343 K)	6
Formula	$C_{36}H_{48}Cl_4Cu_2N_8O_2S_2$	$C_{36}H_{42}Cl_4Cu_2N_{10}$	$C_{38}H_{48}Cl_4Cu_2N_8O_2$	$C_{40}H_{52}Cl_4Cu_2N_8O_2$	$C_{36}H_{46}Cl_4Cu_2N_8O$	$C_{36}H_{46}Cl_4Cu_2N_8O$	$C_{37}H_{50}Cl_4Cu_2N_8$
Formula weight/ $gmol^{-1}$	957.82	883.70	917.74	945.78	866.37	864.01	873.56
Temperature/ K	100(2)	100(2)	100(2)	100(2)	99(2)	343(2)	100(2)
Wavelength/ Å	0.71073	0.71073	0.71073	0.71073	0.71073	0.71073	0.71073
Crystal system	Monoclinic	Monoclinic	Monoclinic	Monoclinic	Monoclinic	Monoclinic	Monoclinic
Space group	$P2_1/c$	$P2_1/c$	$P2_1/c$	$P2_1/c$	$P2_1/c$	$P2_1/c$	$P2_1/c$
a / Å	8.872(2)	8.5707(1)	8.7550(7)	8.860(1)	8.575(4)	8.670(6)	8.499(4)
b / Å	13.043(3)	12.8298(2)	13.3722(1)	13.145(2)	13.295(6)	13.394(5)	13.247(6)
c / Å	17.770(4)	18.181(2)	17.6870(1)	18.080(3)	17.979(8)	18.232(7)	18.335(8)
α / °	90.0	90.0	90.0	90.0	90.0	90.0	90.0
β / °	95.506(3)	91.579(4)	95.982(3)	95.808(2)	95.182(2)	95.236(3)	95.452(9)
γ / °	90.0	90.0	90.0	90.0	90.0	90.0	90.0
V/ $Å^3$	2046.9(7)	1998.4(4)	2059.4(3)	2095.06	2041.54	2108.68	2055.12

3. Thermogravimetric analysis (TGA)

A TGA trace was generated by measuring the percentage mass as the sample was heated at a constant rate. A TA Instruments Q500 thermogravimetric analyser was used. Samples were contained in aluminium pans and sample weights typically ranged from 2 to 5 mg. N_2 gas flowing at a rate of 50 $ml.min^{-1}$ was used to purge the furnace. The temperature was ramped from room temperature to ~500 °C at a constant heating rate of 10 $°C.min^{-1}$. The resulting thermograms were analysed using the TA Instruments Universal Analysis program.

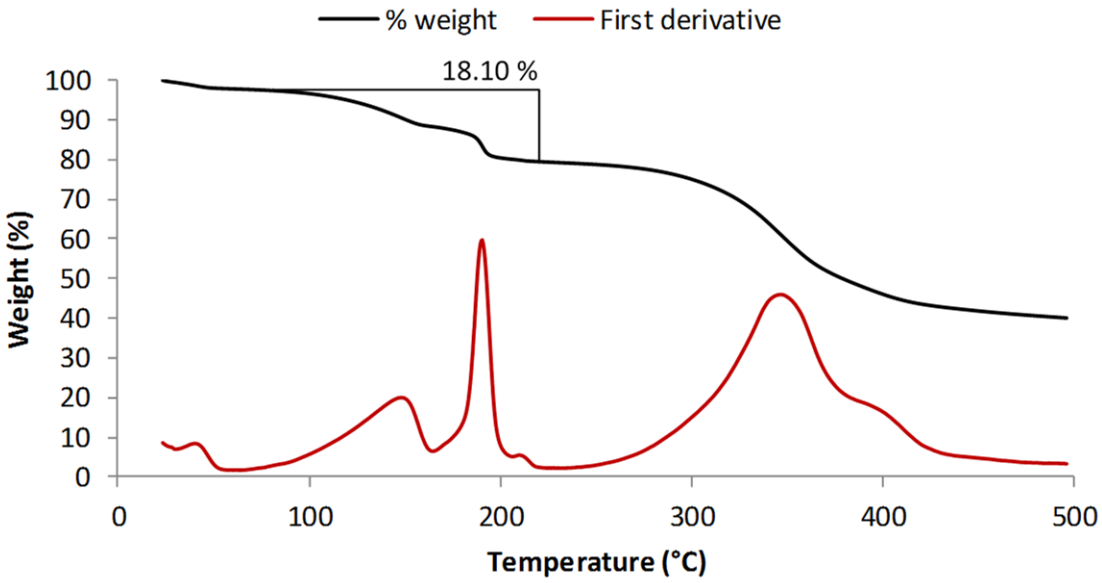

Figure S4: TGA thermogram of **1** showing a net mass loss of 18.10% between 90–220 °C (2 DMSO molecules per metallocycle). The material decomposes at 250 °C.

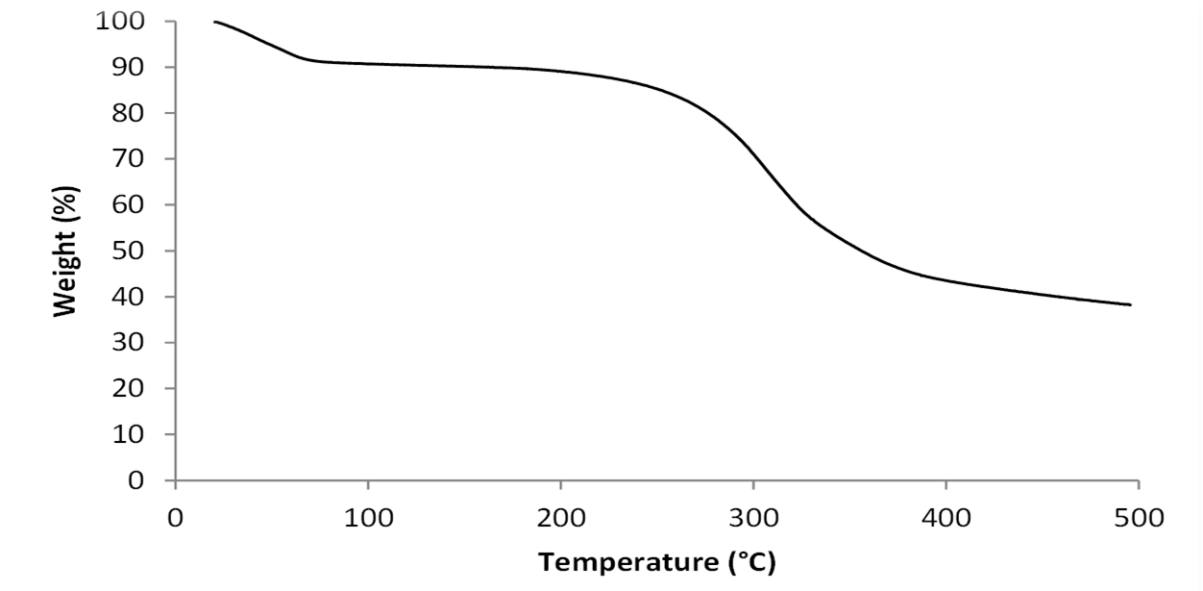

Figure S5: TGA thermogram of 2 showing a net mass loss of 9.174% between 25–33 °C (1 acetonitrile molecule per metallocycle). The material decomposes at 250 °C.

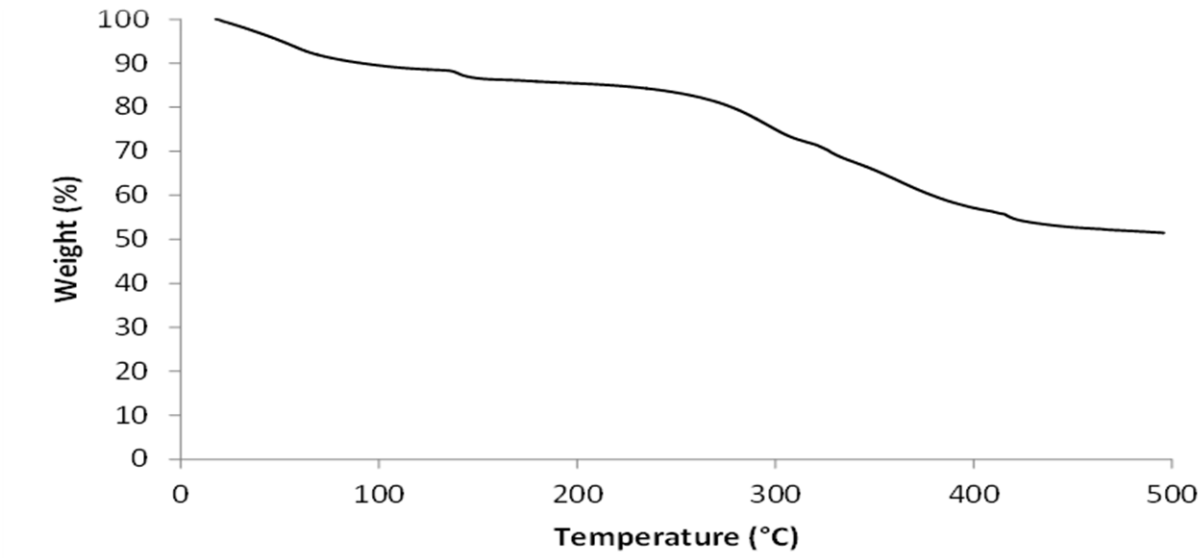

Figure S6: TGA thermogram of 3 showing a net mass loss of 11.321% between 25–48.5 °C (1 acetone molecule per metallocycle). The material decomposes at 250 °C.

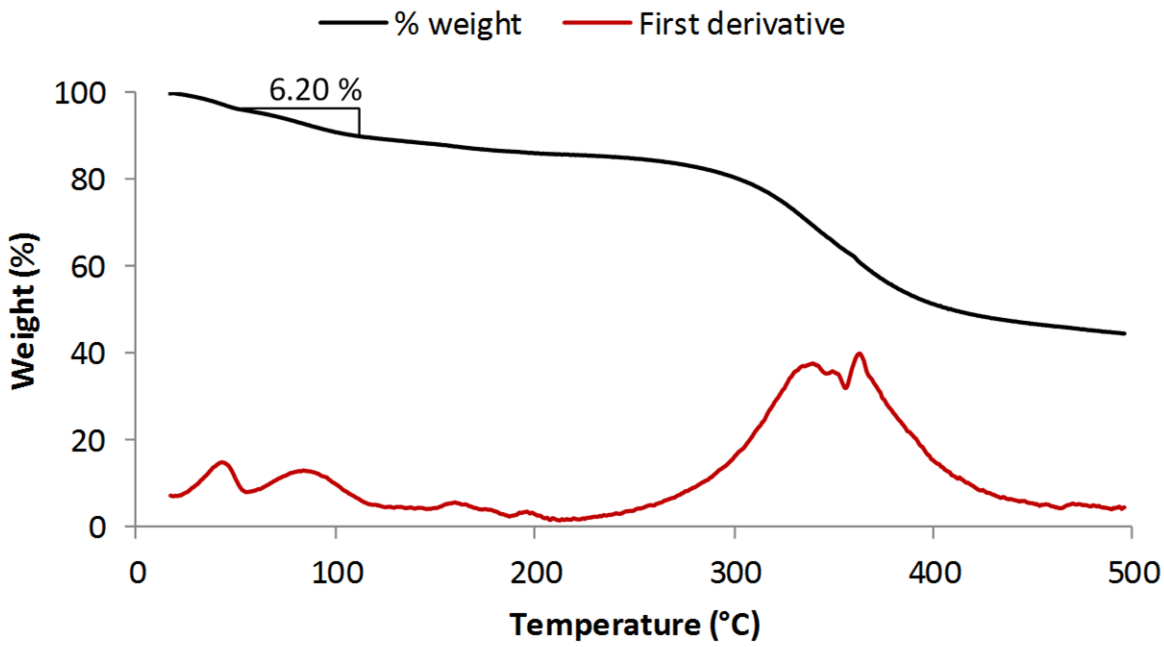

Figure S7: TGA thermogram of **4** showing a net mass loss of 6.20% between 65–118 °C (1 THF molecule per metallocycle). The material decomposes at 250 °C.

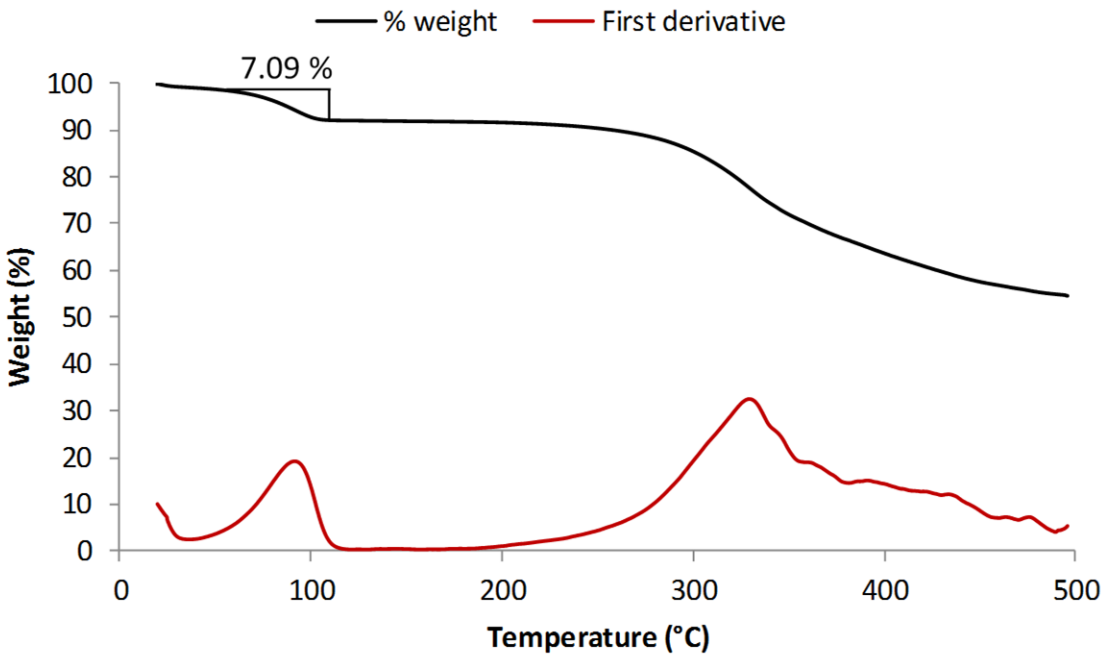

Figure S8: TGA thermogram of **5** showing an initial mass loss 7.09% (1 diethyl ether molecule per metallocycle) over the range 55–119 °C. The material decomposes at 250 °C.

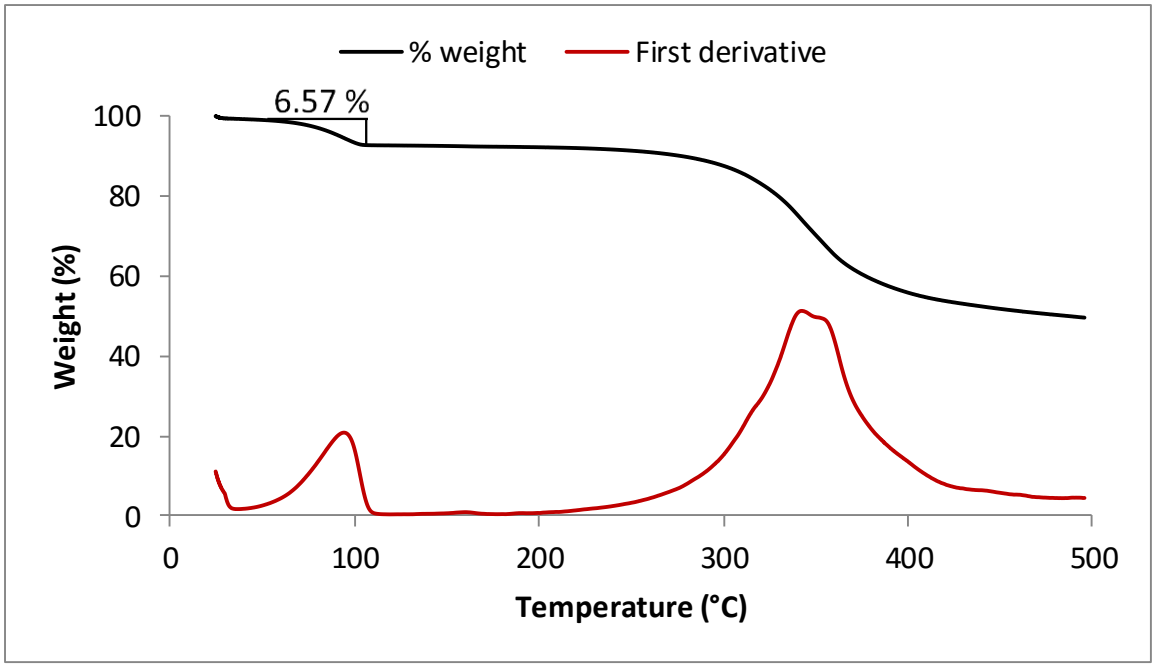

Figure S9: TGA thermogram of **6** showing an initial mass loss of 6.57% (1 pentane molecule per metallocycle) over the range 55–112 °C. The material decomposes at 250 °C.

4. Powder X-ray diffraction (PXRD)

A Bruker D2 Phaser diffractometer was used to record experimental patterns. The diffractometer utilises Bragg-Brentano geometry and Cu Kα radiation (λ = 1.5418 Å) as the incident beam. The diffractometer was operated at 30 kV and 10 mA. Intensity data were recorded using a flat stage. Where necessary samples were finely ground using a mortar and pestle, loaded onto a zero-background sample holder and levelled with a glass slide. The samples were scanned between 5° and 30° or 5° and 35° with a scan step size of 0.016° and a 0.5 second scan speed.

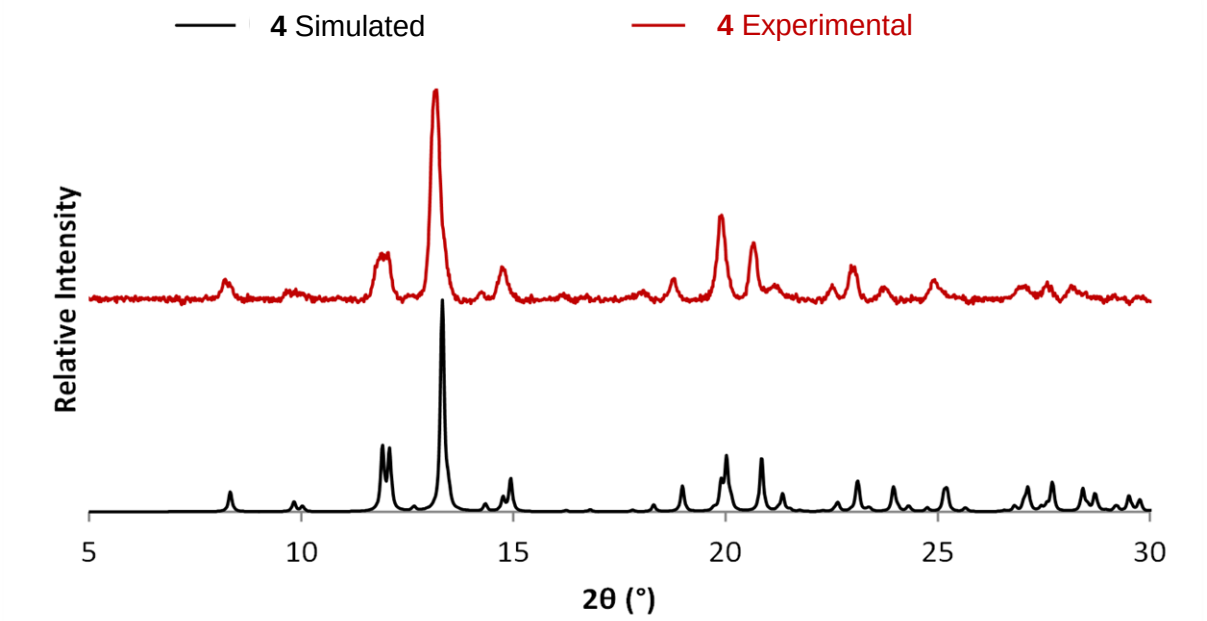

Figure S10: Simulated (black) and experimental (red) PXRD diffractograms of **4**.

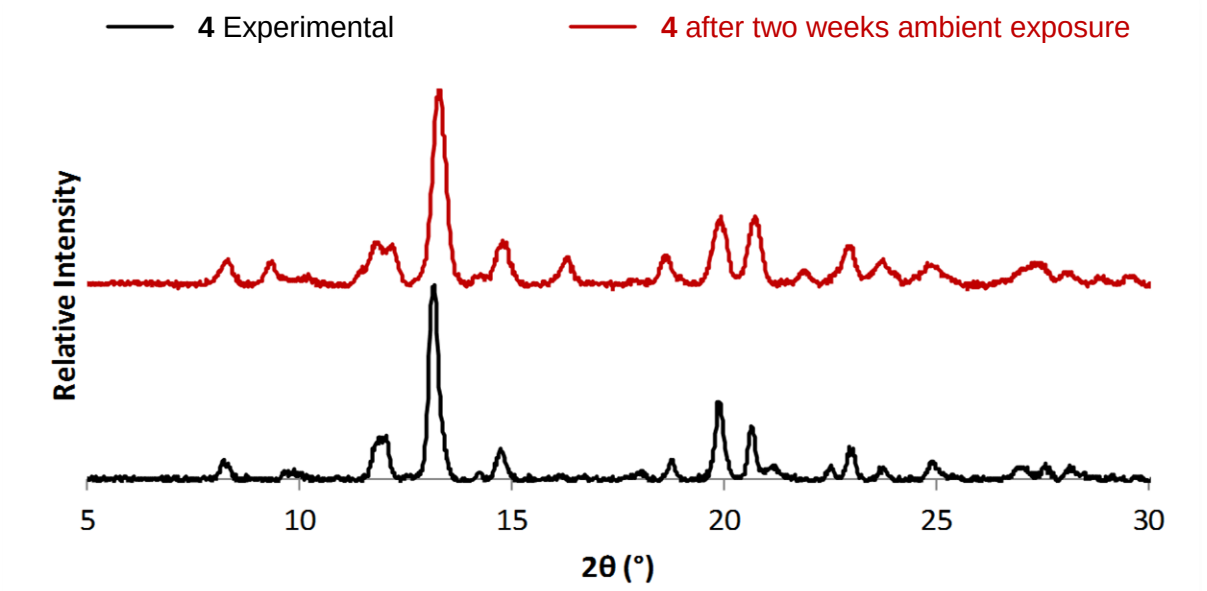

Figure S11: Experimental PXRD diffractograms of **4** (black) and the material after two weeks of ambient conditions (red). Although this does not prove that the guest remains at full occupancy it is clear that the bulk material remains solvated.

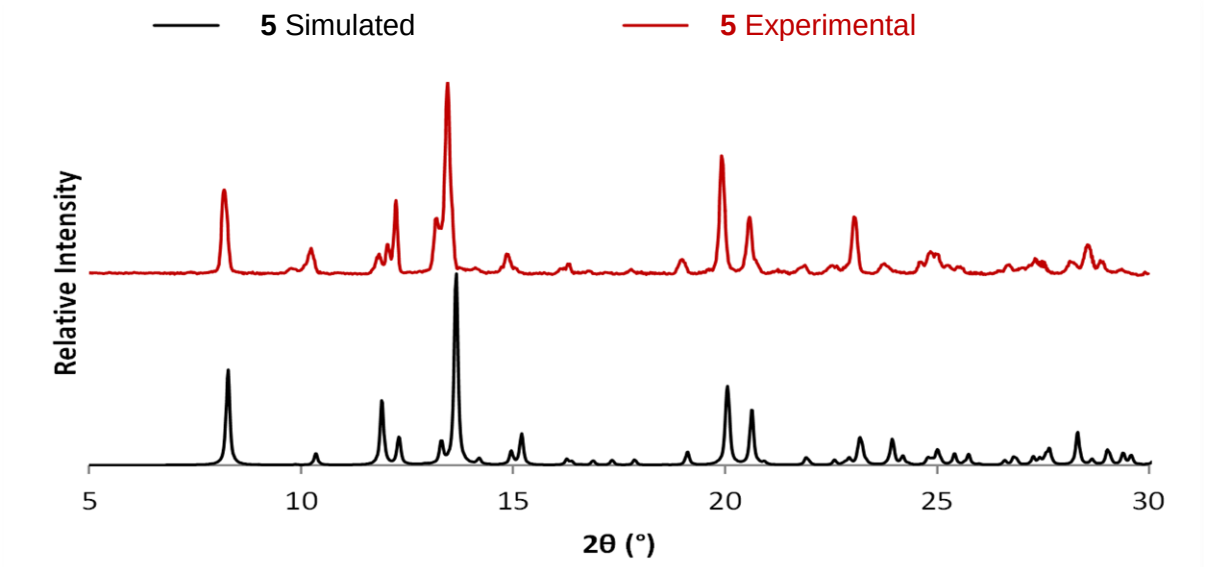

Figure S12: Simulated (black) and experimental (red) PXRD diffractograms of **5**.

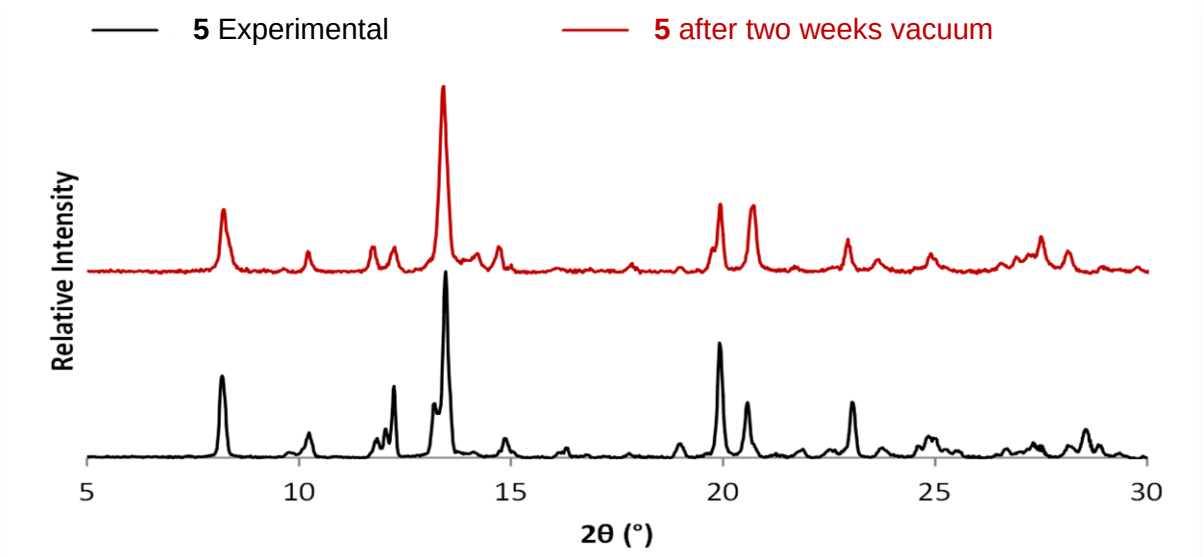

Figure S13: Experimental PXRD diffractograms of **5** (black) and the material after two weeks of vacuum (red). Although this does not prove that the guest remains at full occupancy it is clear that the bulk material remains solvated.

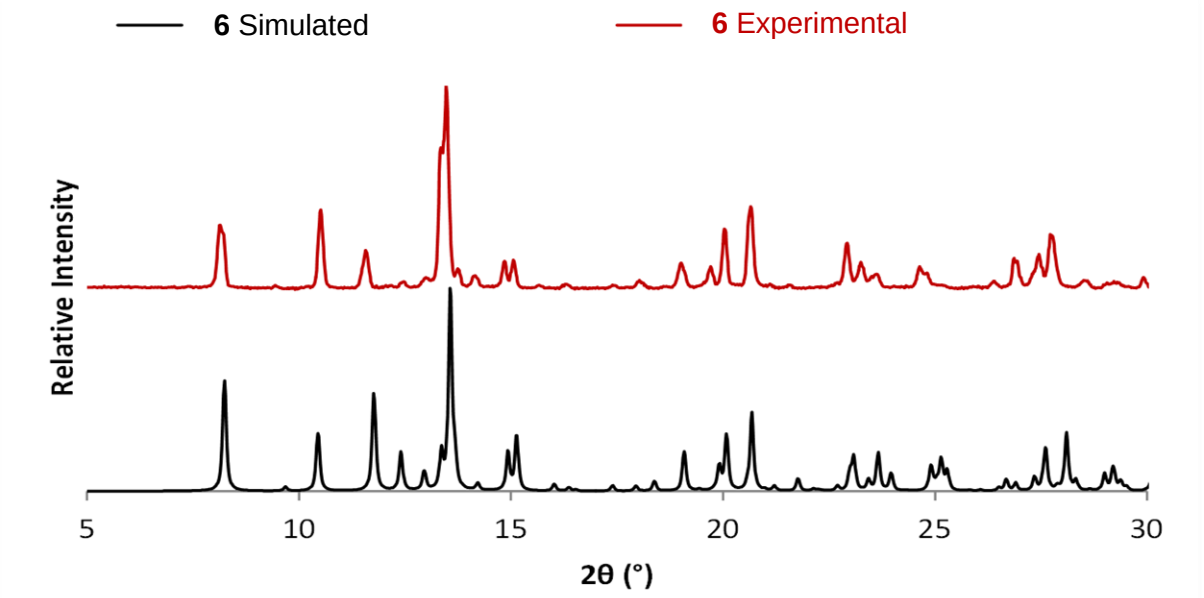

Figure S14: Simulated (black) and experimental (red) PXRD diffractograms of **6.**

5. Electron Paramagnetic Resonance (EPR)

Solid state EPR spectra were recorded on a Bruker EMXplus X-band EPR spectrometer (ca. 9.4 GHz) in the region 295–375 K. The temperature was maintained using a stream of dry nitrogen and a Eurotherm temperature controller. Anisotropic solid state EPR spectra were simulated using PIP [M. Nilges, University of Illinois] via the PIP4WIN GUI [J.M. Rawson, University of Windsor]. EPR spectral simulation parameters for **1**-**6** are given in **Table S2**; those measured by hand are given in **Table S3**.

Table S2: Simulated EPR spectral parameters for metallocycles **1-6.**

1	g_x	g_y	g_z	ΔH_{pp} (x)	ΔH_{pp} (y)	ΔH_{pp} (z)
298(1) K	2.189	2.174	2.091	27	7	15
2						
298(1) K	2.220	2.100	2.140	39	22	29
3						
298(1) K	2.222	2.144	2.098	23	25	21
4						
298(1) K	2.216	2.160	2.090	35	15	12
5						
298(1) K	2.239	2.192	2.106	24	38	28
6						
298(1) K	2.238	2.137	2.094	12	10	12

Table S3: EPR spectral parameters measured directly (by hand) from the derivative absorbance spectra for metallocycles **1-6.**

Solvate	**Cpd.**	**H_x exp. (G)**	**H_y exp. (G)**	**H_z exp. (G)**	**g_x exp.**	**g_y exp.**	**g_z exp.**	**MW Freq. (Hz)**
DMSO	**1**	3215	3270	3369	2.19	2.16	2.09	9.86621
Acetonitrile	**2**	3171	3290	3357	2.22	2.14	2.10	9.86644
Acetone	**3**	3173	3285	3354	2.22	2.14	2.10	9.85967
THF	**4**	3176	3270	3368	2.22	2.16	2.09	9.86385
Ether	**5**	3150	3289	3341	2.24	2.14	2.11	9.86290
Pentane	**6**	3152	3297	3356	2.24	2.14	2.10	9.86108

Table S4: EPR spectral parameters (in units of *g*) from deconvolution (Voigt functions) of the EPR absorption spectra for metallocycles 1-6.[a]

Solvate	Cpd.	g_x^{Abs}	g_y^{Abs}	g_z^{Abs}	$g_x^{Abs} - g_y^{Abs}$	Compo-nent (%)[b]	MW Freq. (Hz)
DMSO	**1**	2.181	2.159	2.105	0.022	100.0	9.86621
Acetonitrile	**2**	2.197	2.133	1.989	0.064	88.4	9.86644
		2.233	2.056	1.891	0.176	11.6	
Acetone	**3**	2.200	2.142	2.108	0.058	~100.0	9.85967
THF	**4**	2.204	2.153	2.101	0.051	78.6	9.86385
		2.12	2.088	2.012	0.032	21.4	
Ether	**5**	2.205	2.136	2.066	0.069	86.4	9.86290
		2.285	2.172	1.977	0.113	13.6	
Pentane	**6**	2.206	2.138	1.988	0.069	60.3	9.86108
		2.213	2.118	1.926	0.095	39.7	

[a] The position of the *g*-value is most accurately determined from the absorption maximum of each of the three tensor components (*x*, y, and z). When an absorption spectrum is plotted in derivative mode, the peaks for g_x and g_z actually correspond to the low-and high-field sides of the respective absorption bands because the change in slope (inflection point) on the side of the band gives the peak in derivative mode. This means that the *g*-values g_x and g_z that are typically measured for a rhombic EPR spectrum *in derivative mode* are *ca.* 1-2% too high and 1-2% too low, respectively. The value measured for g_y is usually the same in derivative and absorption mode spectra (when linewidths are narrow) because the peak maximum in absorbance mode gives a slope of zero in the derivative spectrum. [b] A minor component was present in the spectra of 2, 4, 5, and 6. These components are not easily seen in the derivative spectra since derivative mode plots emphasize regions of rapid change in the absorption envelope. The minor component may be due to a second crystalline phase in the polycrystalline sample or more likely some of the guest-free host (see Figure S15). The presence of the minor component does not greatly affect measurement of the *g*-values.

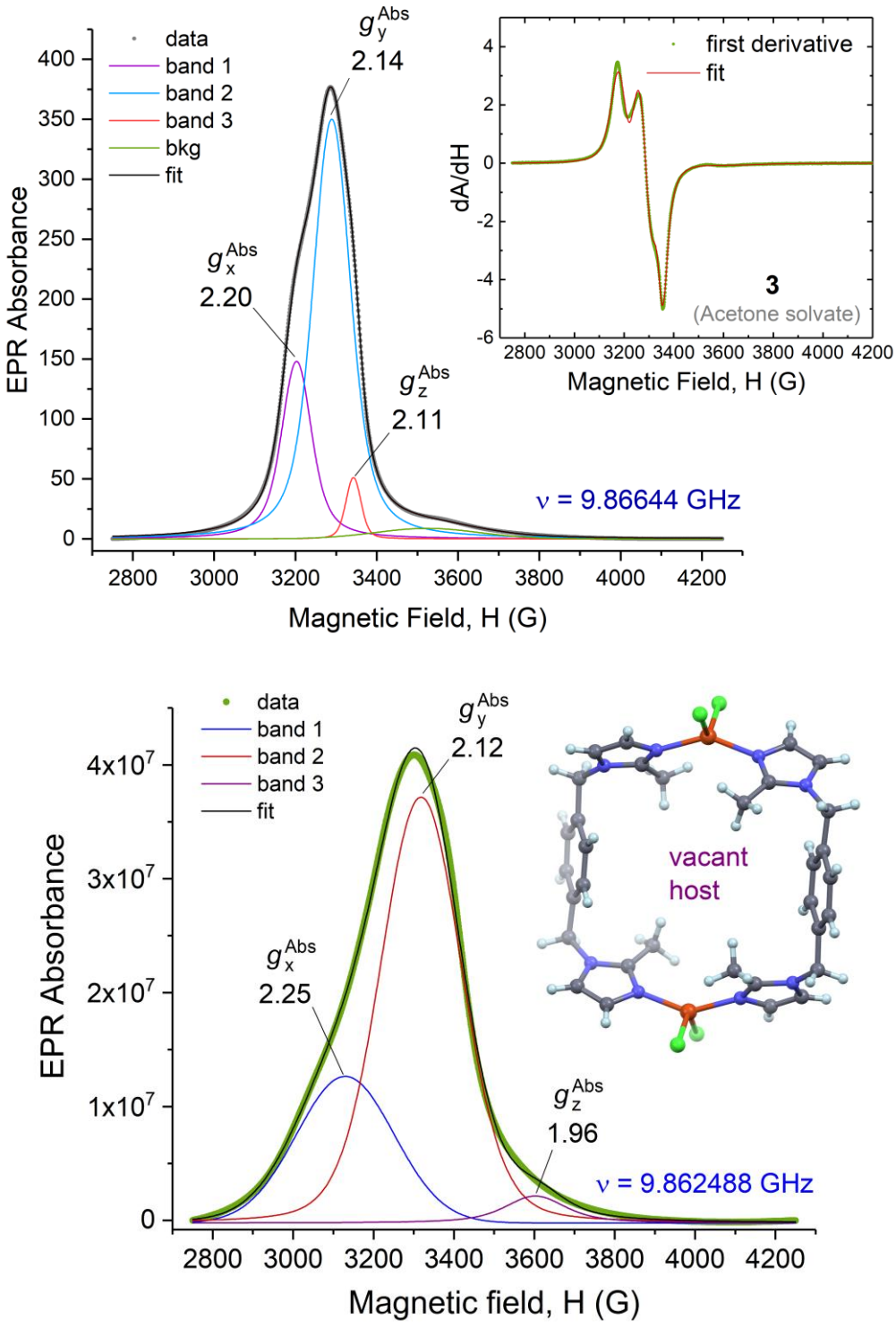

Figure S15: Representative examples of deconvoluted solid-state EPR spectra (absorbance mode) of the solvated metallocycle **3** (upper plot) and the guest-free host metallocycle (lower plot). The host structure has been re-drawn from the atomic coordinates available in the CSD (VERGIJ).[1] Voigt functions were used for spectral deconvolution in both cases; EPR *g*-values have been calculated from the deconvoluted peak maxima ($h\nu = g\beta H$, where h = Plank's constant, H = magnetic field of the absorbance maximum, β = Bohr magneton). The broad signals for the guest-free host reflect the presence of two independent molecules in the asymmetric unit (leading to "*g*-strain"). Attempts to resolve the signals unique to each independent molecule were unsuccessful.

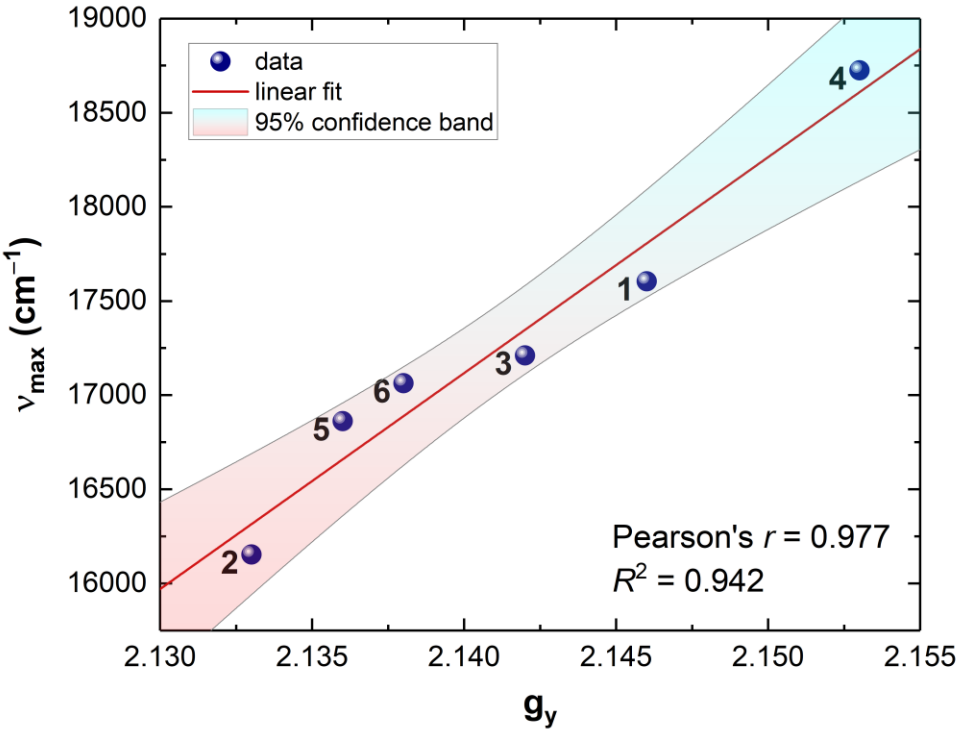

Figure S16: Graph of the correlation between the absorption maximum in the visible electronic spectrum of **1**–**6** and the absorption maximum in the EPR spectrum (g_y) of the host–guest inclusion compounds.

6. Fourier Transform Infrared spectroscopy (FT-IR)

IR absorption spectra were measured using a Nexus Thermo-Nicolet FT-IR instrument with an ATR attachment.

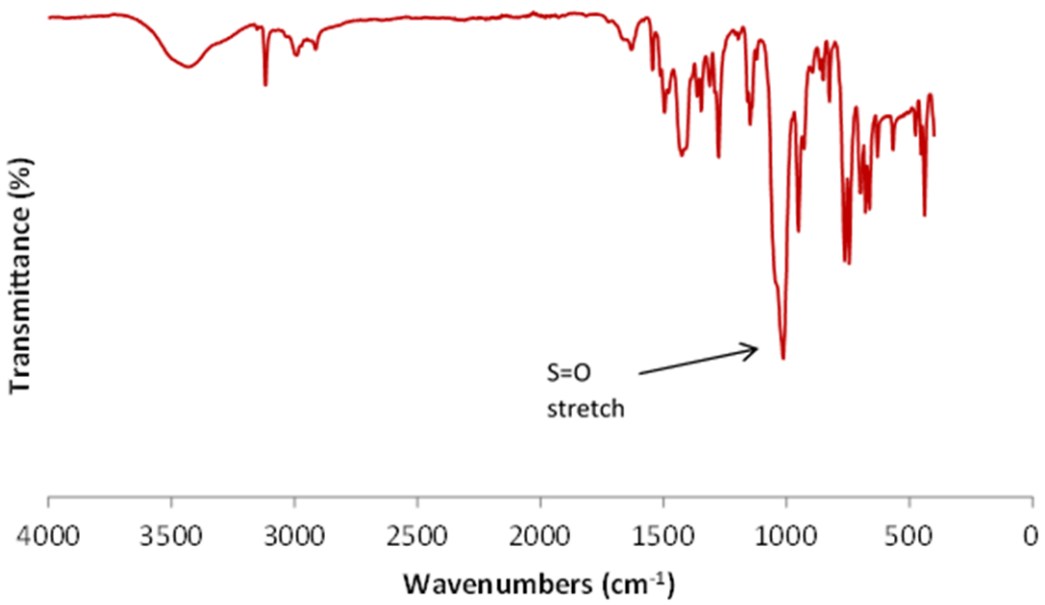

Figure S17: Infrared spectrum of **1.** The S=O stretch of DMSO at ~1000 cm^{-1} is prominent.

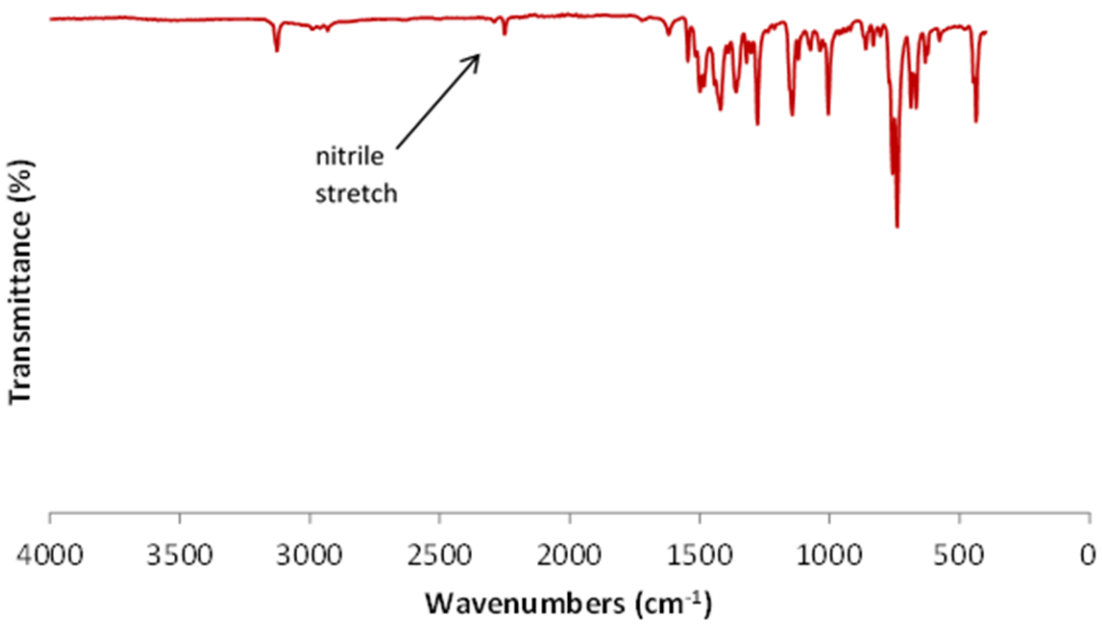

Figure S18: Infrared spectrum of **2.** The nitrile stretch of acetonitrile at ~2250 cm^{-1} is discernible.

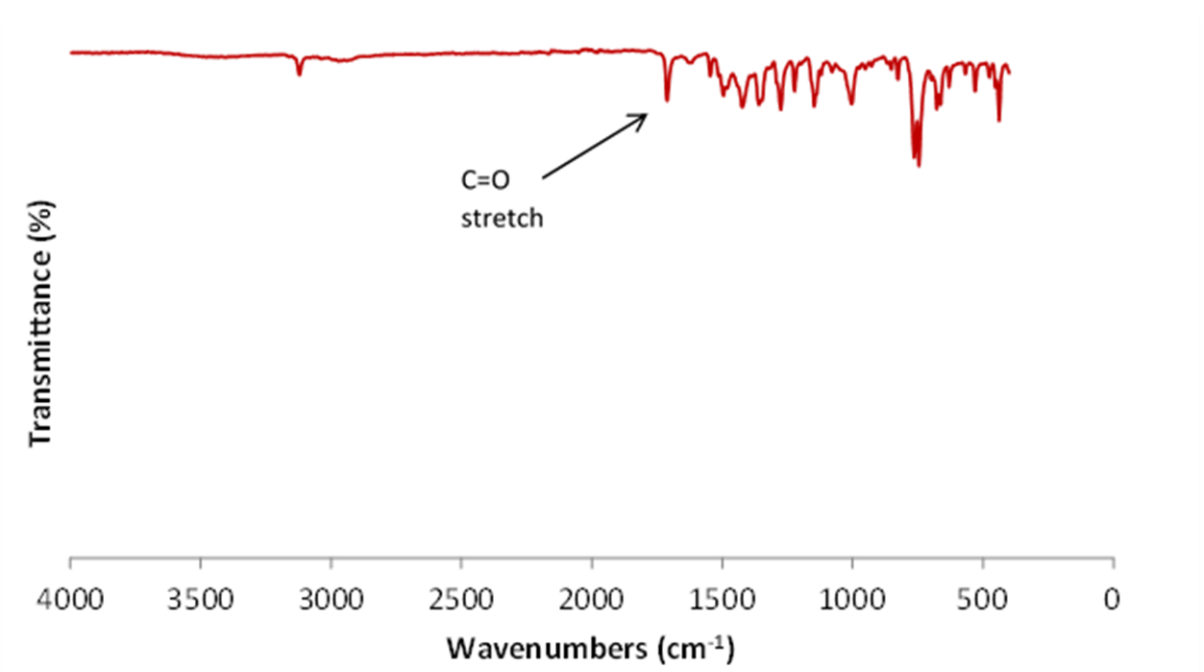

Figure S19: Infrared spectrum of **3**. The C=O stretch of acetone at ~1700 cm^{-1} is distinct.

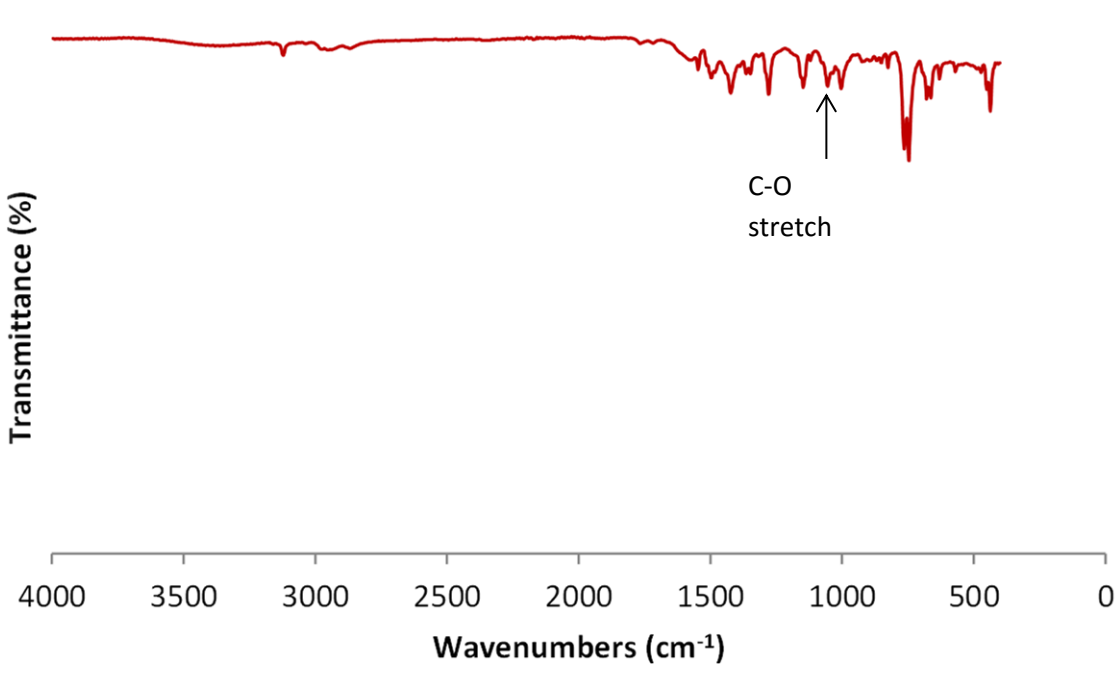

Figure S20: Infrared spectrum of **4.** The C–O stretch just above 1000 cm^{-1} reflects the presence of tetrahydrofuran.

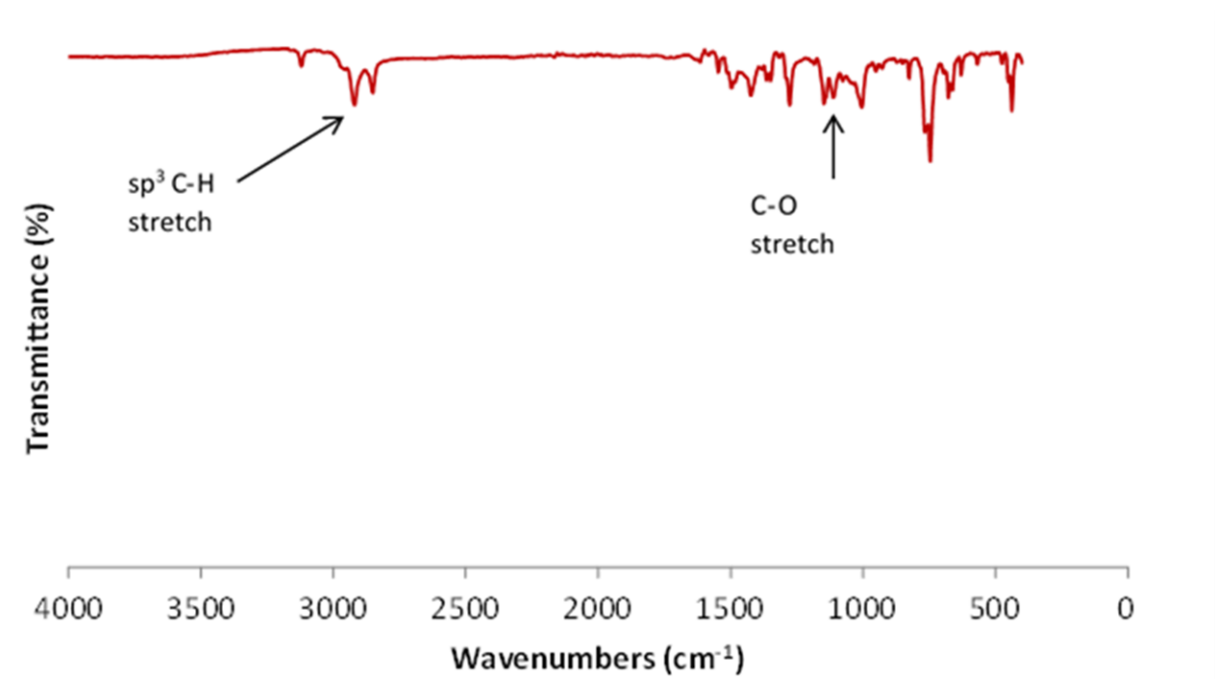

Figure S21: Infrared spectrum of **5** (from **3**). The C–O stretch just above 1000 cm^{-1} and additional sp^3 C–H stretching modes are consistent with the presence of diethylether.

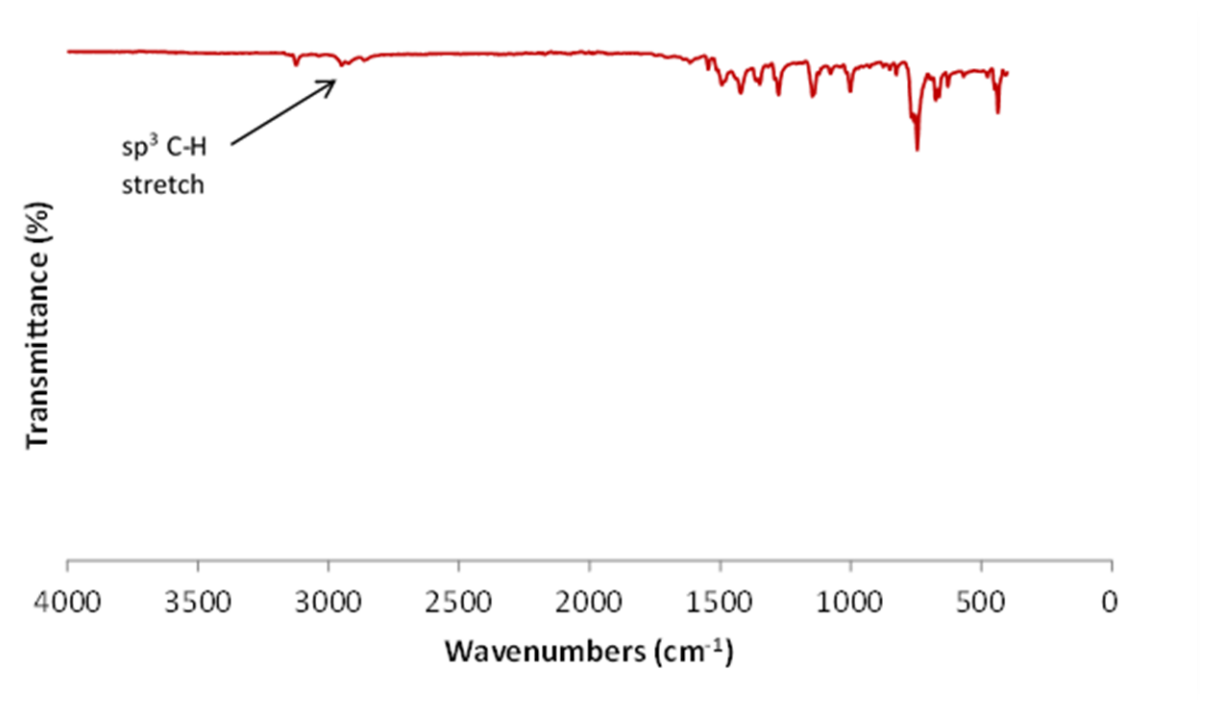

Figure S22: Infrared spectrum of **6**. The presence of sp^3 C–H stretch in modes and the absence of any C–O or C=O peaks indicates inclusion of pentane.

7. Solid-state UV-visible spectroscopy

Solid-state UV-visible absorption spectra were recorded from 350 to 800 nm (1 nm sampling interval) using an Analytik Jena SPECORD 210 PLUS spectrophotometer fitted with an integrating sphere. All measurements were performed in an environment thermostatted within ± 0.1 °C. The data were graphically analysed on the spectrometer using the software package WinAspect PLUS 3.9.14. Spectra for publication were obtained by applying an 8-point fast Fourier transform (FFT) smoothing algorithm to the data before normalization using OriginPro 2017 (64-bit).

Table S5: λ_{max} values for metallocycles **1-6**.

Metallocycle	Crystal Colour	λ_{max} (nm)
1	Green	574
2	Red	624
3	Yellow	588
4	Green	540
5	Orange	598
6	Red-brown	592

8. Density functional theory (DFT) and molecular mechanics calculations

Single Point Energy Calculations: Initially, all non-hydrogen atoms were constrained to their experimental crystallographic positions and hydrogen atoms geometrically optimized as part of a periodic system using the CASTEP module of the Materials Studio software suite.[11] Geometry optimization was performed using the GGA PBE functional[12] with Grimme's DFT-D2 dispersion correction;[13] thresholds for geometry optimization were set at the default fine quality setting. After geometry optimisation of the hydrogen atoms, single point energy calculations were carried out using the same parameters at the ultra-fine quality setting.

Table S6: Single Point Energy Calculations for Selected Solvates.

Solvate	$E_{complex}$ (eV)	E_{host} (eV)	E_{guest} (eV)	$E_{stabilisation}$ (eV)	$E_{stabilisation}$ (kcal/mol)
5	-28 256.23	-25 790.70	-2 462.81	-2.72	-62.73
6	-27 757.93	-25 790.81	-1 964.28	-2.84	-65.49
2	-28 350.90	-25 789.92	-2 558.19	-2.79	-64.34
4	-30 591.36	-25 790.51	-4 796.30	-4.55	-104.93
1	-30 413.49	-25 790.16	-4 618.68	-4.65	-107.23

Radius of Gyration Calculations

The molecular structures of solvents for solvates 1–6 investigated in this work were calculated using the SP4 force field (molecular mechanics)[14] running in VEGA.[15] Regarding calculations of the physical properties of the solvents, VEGA uses an efficient numerical method to calculate the volume of a molecule once the geometry-optimized structure of the molecule has been obtained. The algorithm implemented is based on the robust double cubic lattice method (DCLM) described in the literature,[16] which uses empirical van der Waals radii for the constituent atoms of the molecule and is applicable to both small molecule and macromolecular assemblies. The DCLM also computes molecular surface areas with an input probe radius (typically 1.4 Å for the solvent-accessible surface area) and the volume and compactness of molecular assemblies (without the requirement of an input probe radius). The volume calculated for a molecule by VEGA is thus the van der Waals volume of the molecule and is akin to the solvent-excluded volume defined by Connolly[17] for low molecular weight compounds.

The more important calculated physical parameters for the solvents are listed in Table S7.

Table S7: Calculated Gyration Radii and Other Molecular Parameters for Solvent Guests.[a]

Solvent	Gyration radius/ Å	Surface area/ Å²	Polar area/ Å²	Volume/ Å³	Ovality	Dipole/ Debye
Acetonitrile	1.1820	189.9	60.1	45.9	1.1219	2.2797
DMSO	1.3298	232.8	66.7	72.2	1.2448	8.6172
Acetone	1.3496	215.5	45.0	65.2	1.2267	2.5557
THF	1.3735	242.9	25.8	77.2	1.2215	2.0738
Diethyl ether	1.8555	269.8	13.2	88.4	1.3212	1.7368
Pentane	1.9737	286.6	0.0	97.0	1.3665	0.0023

[a] Surface area calculations were performed with a probe radius of 1.4 Å. The volume of the molecule is the calculated van der Waals volume based on van der Waals radii for the constituent atoms.

Time Dependant Density Functional Theory (TD-DFT) Calculations: These were performed with Gaussian 09 Revision E.01[18] at the HSEH1PBE[19]/6-311g(d,p)[20] level of theory on single metallocycles and their guests taken from the asymmetric unit of each crystal structure. Because the lattice was not included in the calculations (TD-DFT calculations on three-dimensional solids using periodic boundary conditions based on the unit cell are not currently implementable in Gaussian) we elected to embed each metallocycle inclusion compound in a uniform dielectric environment of moderate polarity (THF) using a standard solvation model (PCM[21]) for the spectral simulations. THF was chosen as solvate **4** contains THF and we wanted a uniform background environment for the calculations on all compounds. The system in each case behaves as a spin triplet in the ground state (two isolated spins on each Cu^{2+} ion). A total of 70 excited triplet states were selected for solution to locate the spin-allowed bands. Calculations were performed in both C1 symmetry (no constraints) and Ci symmetry (where such symmetry was possible). Symmetrisation of the structure had a negligible effect on the calculated electronic spectra. The electronic spectra were analysed with GaussSum 3.0.[22] We also checked the effect of the PCM environment on the calculated excited states by comparing those determined for **2** in a THF continuum to those calculated with an *in vacuo* model of the same system. The identity and intensities of lowest-energy excited states were essentially equivalent in both models; those determined *in vacuo* were, however, typically around 14–76 nm lower in energy than those determined in the THF continuum.

All three-dimensional surfaces (spin density, molecular orbitals) were visualized and rendered with isosurfaces of ±0.02 au (default value) using GausView 5.0.9.[23]

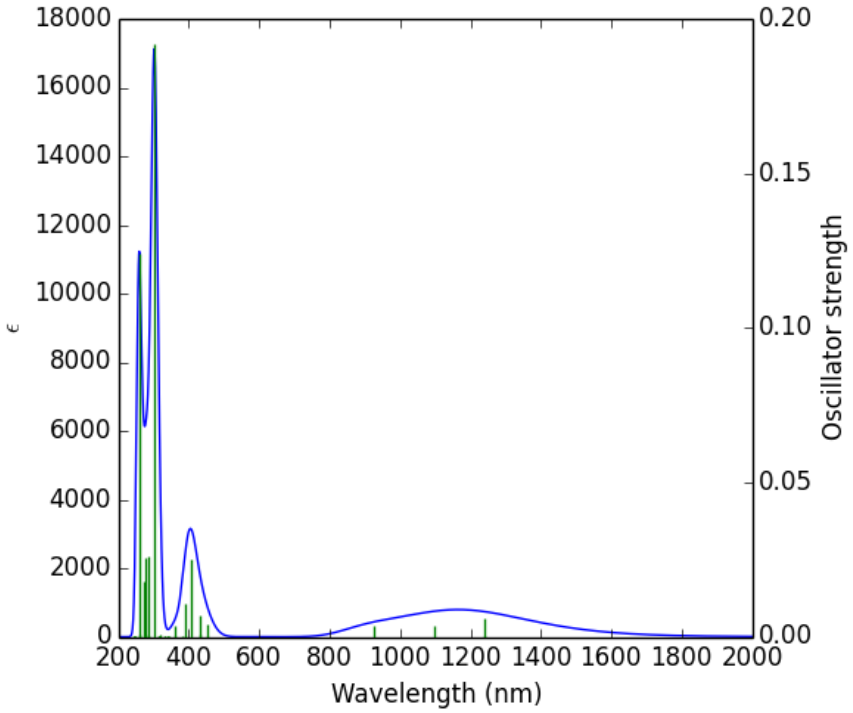

Figure S23: Simulated UV-vis-NIR spectra of **2** (THF solvent continuum, Ci symmetry).

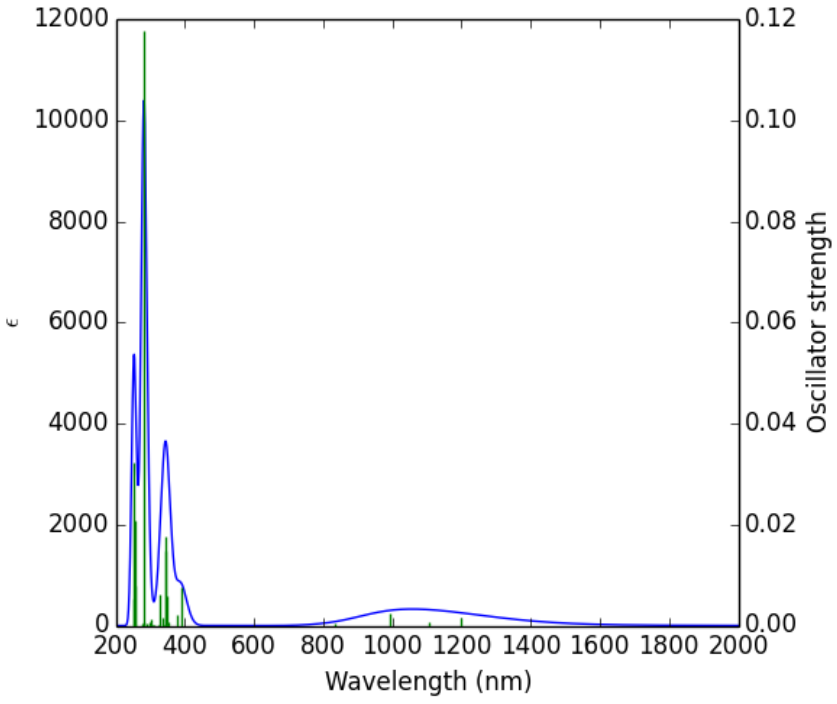

Figure S24: Simulated UV-vis-NIR spectra of **3** (THF solvent continuum, Ci symmetry).

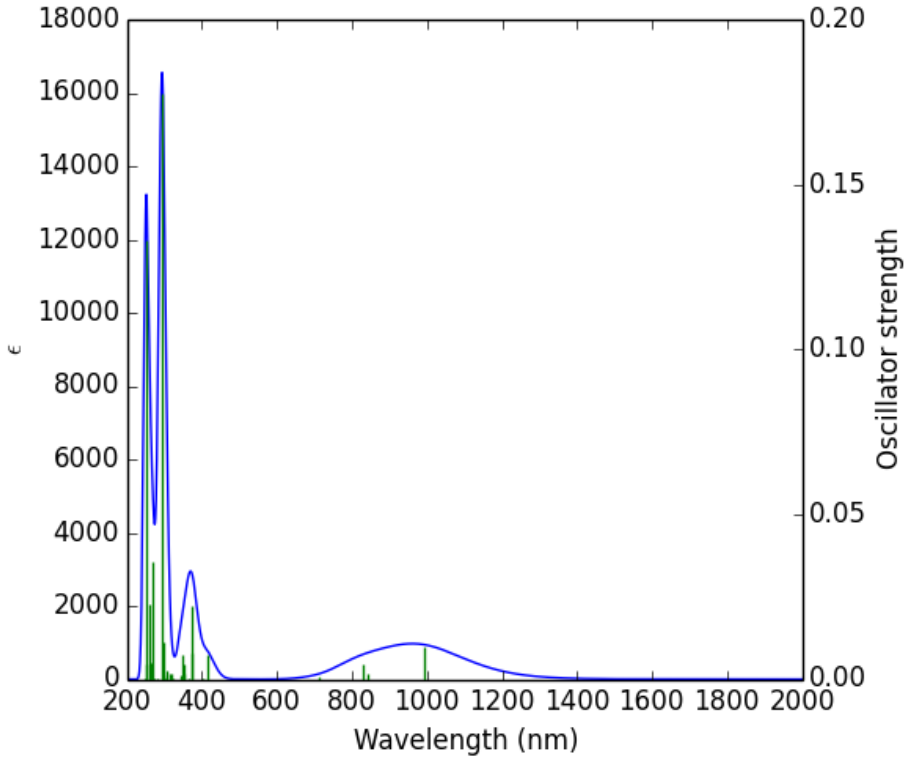

Figure S25: Simulated UV-vis-NIR spectra of **4** (THF solvent continuum, Ci symmetry).

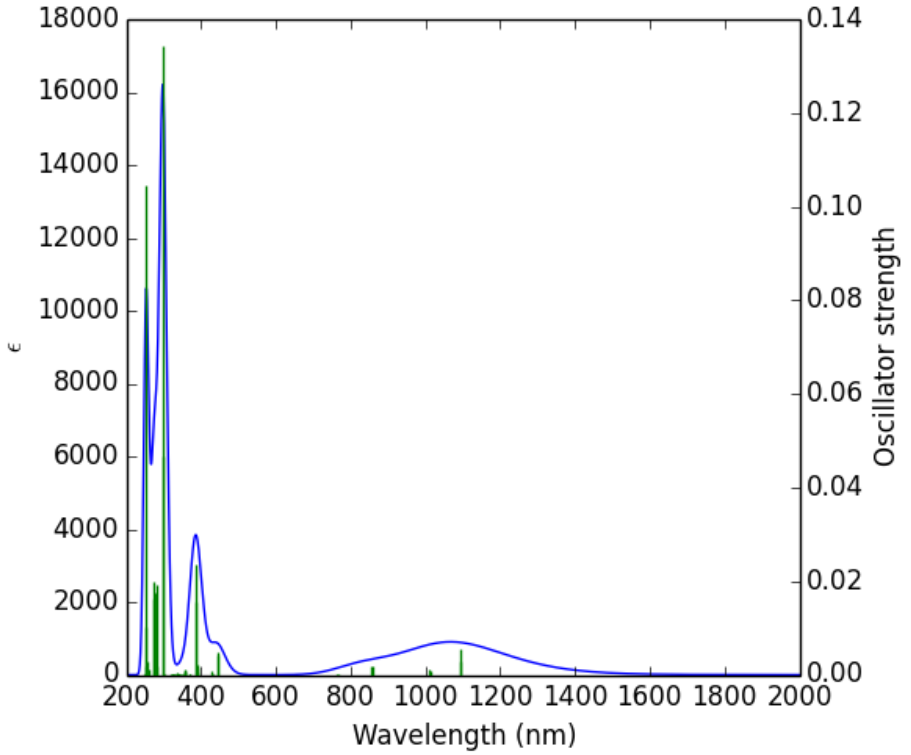

Figure S26: Simulated UV-vis-NIR spectra of **5** (THF continuum, C1 symmetry).

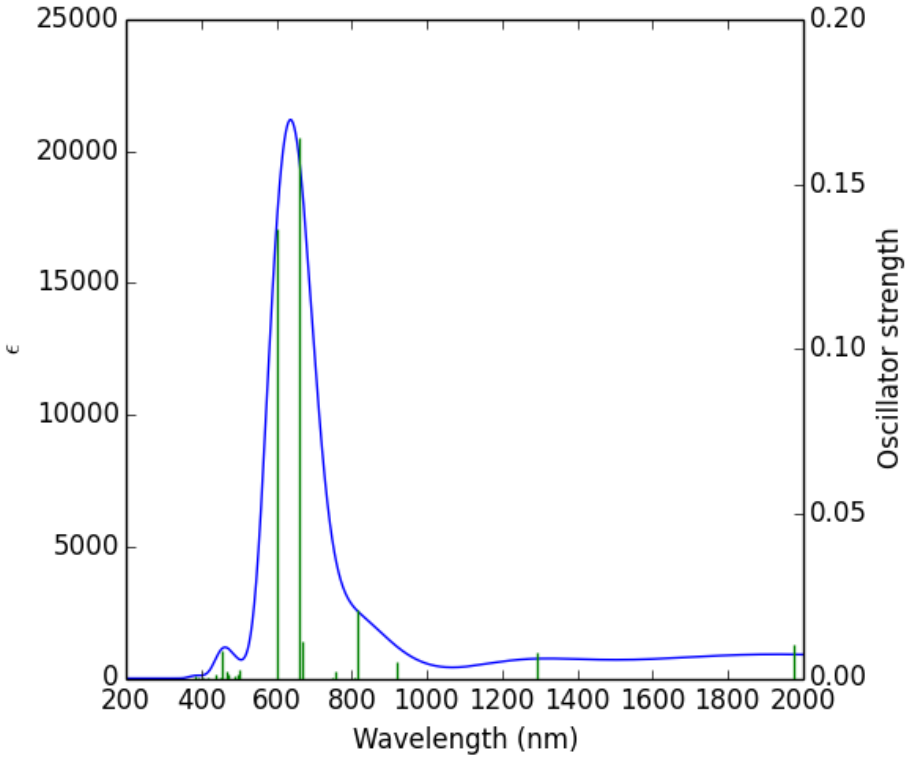

Figure S27: Simulated UV-vis-NIR spectra of **6** (THF solvent continuum, Ci symmetry).

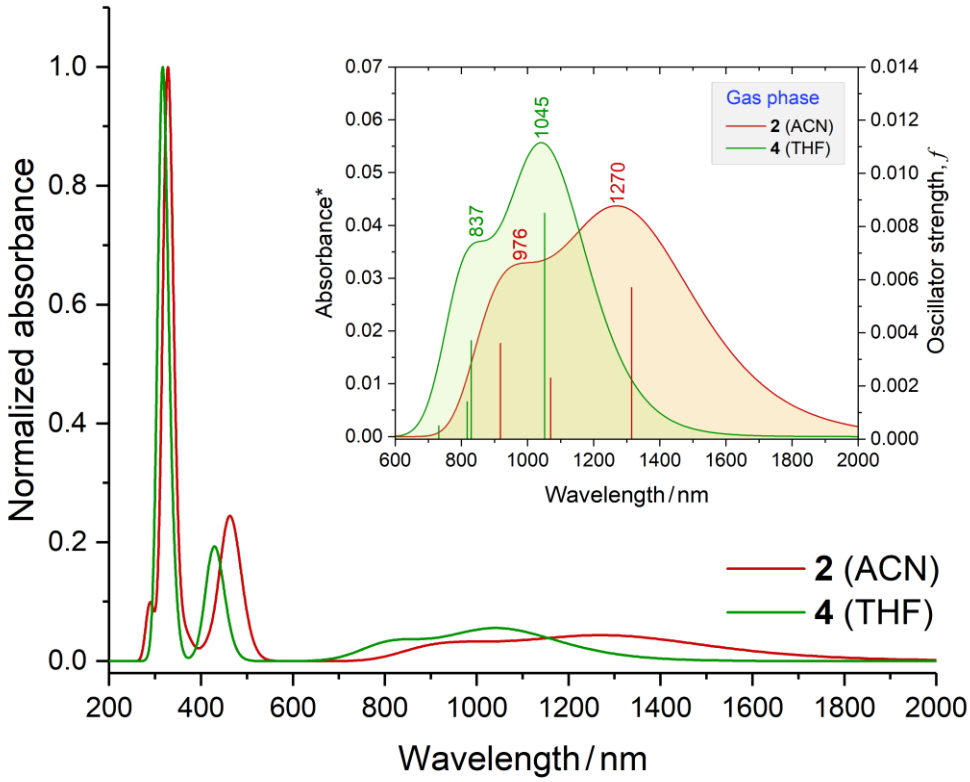

Figure S28: Comparison of the normalized *in vacuo* TD-DFT calculated electronic absorption spectra of **2** and **4** (Ci symmetry). The inset compares the lowest-energy transitions for the two solvates. Although the absolute wavelengths of the DFT-calculated band maxima are longer (~500 nm) than those observed experimentally, the calculations correctly predict that the electronic spectrum of the THF solvate will be blue-shifted relative to that of the acetonitrile solvate. The calculated blue-shift is *ca.* 225 nm in the gas phase (based on the transition energy of the longest-wavelength band).

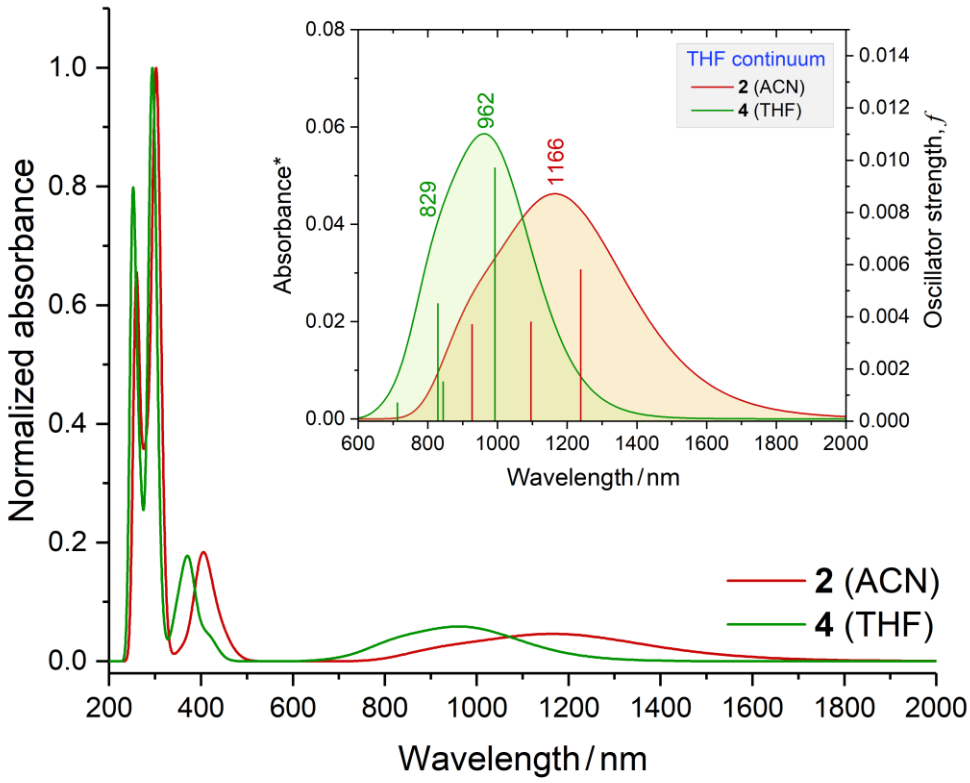

Figure S29: Comparison of the normalized TD-DFT calculated electronic absorption spectra of **2** and **4** (THF solvent continuum). The inset compares the lowest-energy transitions for the two solvates. Although the absolute wavelengths of the DFT-calculated band maxima are longer by 420 nm (**4**) and 542 nm (**2**) than those observed experimentally, the calculations correctly predict that the electronic spectrum of the THF solvate will be blue-shifted relative to that of the acetonitrile solvate. The calculated blue-shift is *ca.* 204 nm in a THF solvent continuum (based on the transition energy of the longest-wavelength band).

Table S8: List of the twelve lowest-energy transitions (out of 70 excited states) calculated for **metallocycle 2** (**Ci symmetry, gas phase**) for the purpose of illustration and assignment of the key transitions contributing to the electronic absorption spectrum in the visible region. Note that the DFT-calculated wavelengths are approximately 500 nm to the red of the experimental transitions.[a]

Wavelength (nm)	***f*** [b]	**Symmetry**	**Major contributions** [c]							
1314.8	0	^3A_g	H-29(B) → LUMO(B)	(13%)	H-28(B) → L+1(B)	(13%)	H-1(B) → L+1(B)	(29%)	HOMO(B) → LUMO(B)	(29%)
1314.8	**0.0057**	**^3A_u**	**H-29(B) → L+1(B)**	**(13%)**	**H-28(B) → LUMO(B)**	**(13%)**	**H-1(B) → LUMO(B)**	**(29%)**	**HOMO(B) → L+1(B)**	**(29%)**
1071.0	0	^3A_g	H-16(B) → L+1(B)	(17%)	H-39(B) → L+1(B)	(4%)	H-37(B) → LUMO(B)	(3%)	H-26(B) → LUMO(B)	(3%)
1070.0	**0.0023**	**^3A_u**	**H-16(B) → LUMO(B)**	**(17%)**	**H-39(B) → LUMO(B)**	**(4%)**	**H-37(B) → L+1(B)**	**(3%)**	**H-26(B) → L+1(B)**	**(3%)**
917.9	**0.0036**	**^3A_u**	**H-27(B) → LUMO(B)**	**(16%)**	**H-25(B) → L+1(B)**	**(13%)**	**H-7(B) → L+1(B)**	**(18%)**	**H-6(B) → LUMO(B)**	**(18%)**
917.6	0	^3A_g	H-27(B) → L+1(B)	(16%)	H-25(B) → LUMO(B)	(13%)	H-7(B) → LUMO(B)	(18%)	H-6(B) → L+1(B)	(18%)
832.2	0	^3A_u	H-35(B) → LUMO(B)	(20%)	H-34(B) → L+1(B)	(20%)	H-5(B) → LUMO(B)	(11%)	H-4(B) → L+1(B)	(11%)
832.2	0	^3A_g	H-35(B) → L+1(B)	(20%)	H-34(B) → LUMO(B)	(20%)	H-5(B) → L+1(B)	(11%)	H-4(B) → LUMO(B)	(11%)
465.9	0	^3A_g	H-9(B) → LUMO(B)	(19%)	H-8(B) → L+1(B)	(19%)	H-3(B) → L+1(B)	(10%)	H-2(B) → LUMO(B)	(10%)
465.8	0.0261	^3A_u	H-9(B) → L+1(B)	(19%)	H-8(B) → LUMO(B)	(19%)	H-3(B) → LUMO(B)	(10%)	H-2(B) → L+1(B)	(10%)
456.2	0	^3A_g	H-9(B) → LUMO(B)	(10%)	H-8(B) → L+1(B)	(10%)	H-3(B) → L+1(B)	(12%)	H-2(B) → LUMO(B)	(13%)
456.1	0.0105	^3A_u	H-8(B) → LUMO(B)	(10%)	H-3(B) → LUMO(B)	(12%)	H-2(B) → L+1(B)	(12%)	H-29(B) → L+1(B)	(2%)

[a] HOMO (A): 228; HOMO (B): 226. The three main transitions responsible for the colour of the metallocycle solvate are given in bold colour typeface. [b] Oscillator strength. [c] A and B refer to alpha and beta spin orbitals, respectively. HOMO, H; LUMO, L.

Table S9: List of the twelve lowest-energy transitions (out of 70 excited states) calculated for **metallocycle 2** (**Ci symmetry, THF solvent continuum**) for the purpose of illustration and assignment of the key transitions contributing to the electronic absorption spectrum in the visible region. Note that the DFT-calculated wavelengths are approximately 500 nm to the red of the experimental transitions.[a]

Wavelength (nm)	***f*** [b]	**Symmetry**	**Major contributions** [c]							
1239.0	0	^3A_g	H-35(B) → L+1(B)	(10%)	H-34(B) → LUMO(B)	(11%)	H-5(B) → L+1(B)	(20%)	H-4(B) → LUMO(B)	(22%)
1238.6	**0.006**	**^3A_u**	**H-35(B) → LUMO(B)**	**(10%)**	**H-34(B) → L+1(B)**	**(11%)**	**H-5(B) → LUMO(B)**	**(20%)**	**H-4(B) → L+1(B)**	**(22%)**
1096.4	0	^3A_g	H-19(B) → LUMO(B)	(10%)	H-18(B) → L+1(B)	(11%)	H-7(B) → L+1(B)	(10%)	H-6(B) → LUMO(B)	(15%)
1095.9	**0.0038**	**^3A_u**	**H-19(B) → L+1(B)**	**(10%)**	**H-18(B) → LUMO(B)**	**(11%)**	**H-7(B) → LUMO(B)**	**(10%)**	**H-6(B) → L+1(B)**	**(15%)**
926.9	**0.0037**	**^3A_u**	**H-29(B) → L+1(B)**	**(15%)**	**H-28(B) → LUMO(B)**	**(14%)**	**H-13(B) → LUMO(B)**	**(10%)**	**H-12(B) → L+1(B)**	**(17%)**
926.63	0	^3A_g	H-29(B) → LUMO(B)	(15%)	H-28(B) → L+1(B)	(14%)	H-13(B) → L+1(B)	(10%)	H-12(B) → LUMO(B)	(17%)
794.8	0	^3A_u	H-41(B) → L+1(B)	(19%)	H-40(B) → LUMO(B)	(25%)	H-9(B) → L+1(B)	(15%)	H-36(B) → L+1(B)	(6%)
794.8	0	^3A_g	H-41(B) → LUMO(B)	(19%)	H-40(B) → L+1(B)	(25%)	H-9(B) → LUMO(B)	(15%)	H-36(B) → LUMO(B)	(6%)
452.3	0	^3A_g	H-1(B) → L+1(B)	(46%)	HOMO(B) → LUMO(B)	(47%)				
452.2	0.0042	^3A_u	H-1(B) → LUMO(B)	(47%)	HOMO(B) → L+1(B)	(47%)				
431.8	0	^3A_g	H-3(B) → LUMO(B)	(39%)	H-2(B) → L+1(B)	(37%)	H-11(B) → LUMO(B)	(2%)	H-7(B) → L+1(B)	(4%)
431.7	0.0072	^3A_u	H-3(B) → L+1(B)	(39%)	H-2(B) → LUMO(B)	(37%)	H-11(B) → L+1(B)	(2%)	H-7(B) → LUMO(B)	(4%)

[a] HOMO (A): 228; HOMO (B): 226. The three main transitions responsible for the colour of the metallocycle solvate are given in bold colour typeface. [b] Oscillator strength. [c] A and B refer to alpha and beta spin orbitals, respectively. HOMO, H; LUMO, L.

Table S10: List of the twelve lowest-energy transitions (out of 70 excited states) calculated for metallocycle 4 (Ci symmetry, THF solvent continuum) for the purpose of illustration and assignment of the key transitions contributing to the electronic absorption spectrum in the visible region. Note that the DFT-calculated wavelengths are approximately 500 nm to the red of the experimental transitions.[a]

Wavelength (nm)	f [b]	Symmetry	Major contributions [c]							
993.0	0	^3A_g	H-37(B) → LUMO(B)	(16%)	H-36(B) → L+1(B)	(15%)	H-5(B) → LUMO(B)	(26%)	H-4(B) → L+1(B)	(26%)
992.8	**0.0097**	**^3A_u**	**H-37(B) → L+1(B)**	**(16%)**	**H-36(B) → LUMO(B)**	**(15%)**	**H-5(B) → L+1(B)**	**(26%)**	**H-4(B) → LUMO(B)**	**(26%)**
843.78	0	^3A_g	H-29(B) → LUMO(B)	(10%)	H-28(B) → L+1(B)	(10%)	H-21(B) → LUMO(B)	(13%)	H-20(B) → L+1(B)	(14%)
843.68	**0.0015**	**^3A_u**	**H-28(B) → LUMO(B)**	**(10%)**	**H-21(B) → L+1(B)**	**(13%)**	**H-20(B) → LUMO(B)**	**(14%)**	**H-9(B) → L+1(B)**	**(10%)**
829.0	**0.0045**	**^3A_u**	**H-31(B) → LUMO(B)**	**(15%)**	**H-30(B) → L+1(B)**	**(15%)**	**H-25(B) → LUMO(B)**	**(10%)**	**H-24(B) → L+1(B)**	**(10%)**
828.7	0	^3A_g	H-31(B) → L+1(B)	(15%)	H-30(B) → LUMO(B)	(15%)	H-25(B) → L+1(B)	(10%)	H-24(B) → LUMO(B)	(10%)
712.3	0	^3A_g	H-44(B) → L+1(B)	(12%)	H-43(B) → LUMO(B)	(17%)	H-48(B) → L+1(B)	(5%)	H-46(B) → LUMO(B)	(4%)
712.3	**0.0007**	**^3A_u**	**H-44(B) → LUMO(B)**	**(12%)**	**H-43(B) → L+1(B)**	**(17%)**	**H-48(B) → LUMO(B)**	**(5%)**	**H-46(B) → L+1(B)**	**(4%)**
415.8	0	^3A_g	H-3(B) → L+1(B)	(25%)	H-2(B) → LUMO(B)	(16%)	H-1(B) → LUMO(B)	(24%)	HOMO(B) → L+1(B)	(13%)
415.7	0.0074	^3A_u	H-3(B) → LUMO(B)	(25%)	H-2(B) → L+1(B)	(15%)	H-1(B) → L+1(B)	(24%)	HOMO(B) → LUMO(B)	(14%)
404.4	0.0004	^3A_u	H-3(B) → LUMO(B)	(16%)	H-2(B) → L+1(B)	(27%)	H-1(B) → L+1(B)	(17%)	HOMO(B) → LUMO(B)	(33%)
404.4	0	^3A_g	H-3(B) → L+1(B)	(15%)	H-2(B) → LUMO(B)	(27%)	H-1(B) → LUMO(B)	(18%)	HOMO(B) → L+1(B)	(32%)

[a] HOMO (A): 246; HOMO (B): 244. The four main transitions responsible for the colour of the metallocycle solvate are given in bold colour typeface. [b] Oscillator strength. [c] A and B refer to alpha and beta spin orbitals, respectively. HOMO, H; LUMO, L.

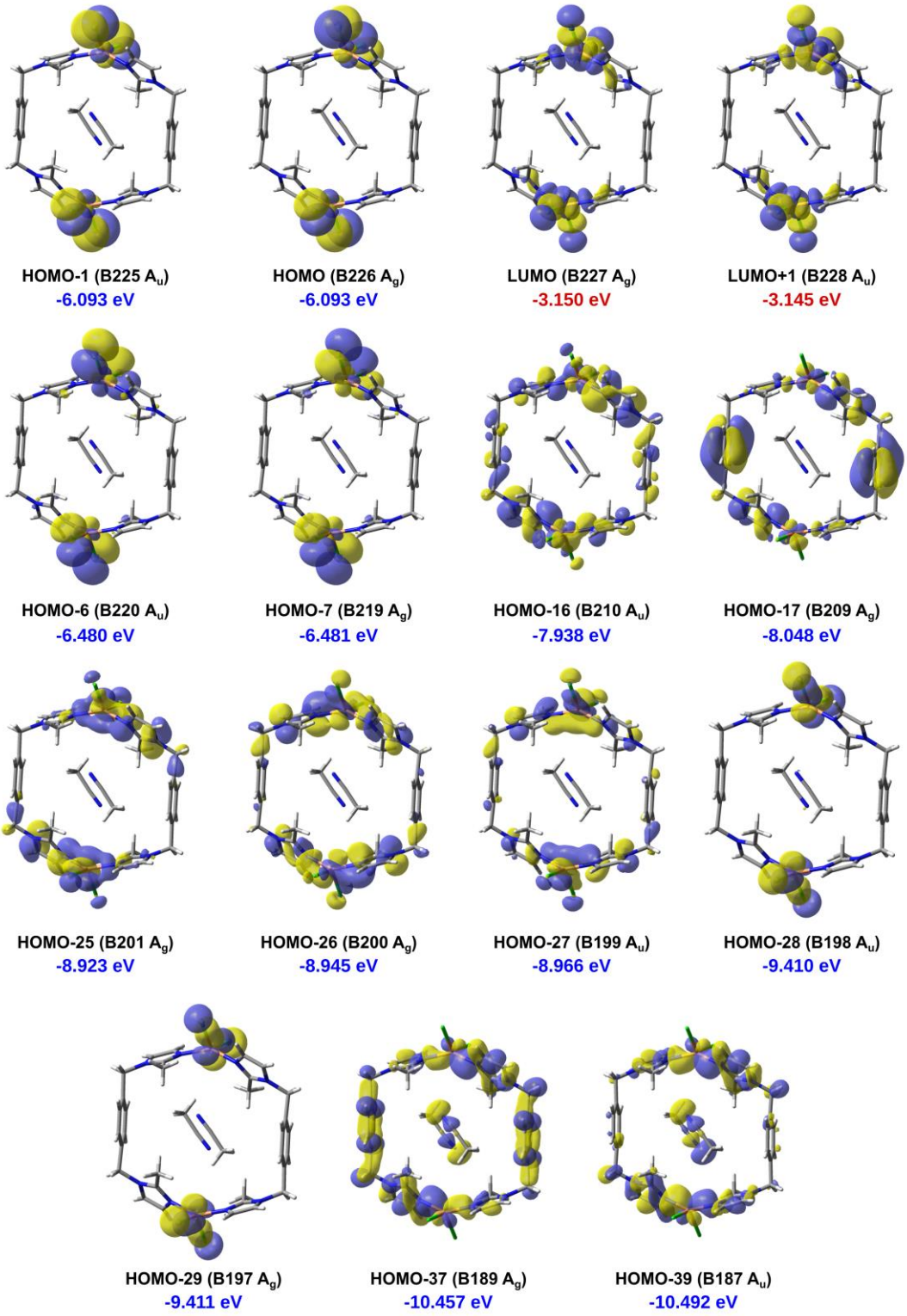

Figure S30: Main molecular orbitals of **2** (Ci symmetry, gas phase, β-spin) involved in the lowest-energy transitions calculated by TD-DFT and highlighted in **Table S8**. Based on the transition identities in **Table S8** and the MOs involved, the transitions responsible for the colour of the metallocycles have mainly d–d character (as expected from ligand field theory) since the metal atomic orbitals show only a relatively minor admixture with ligand framework orbitals. A good example of a nearly pure metal atomic orbital is MO B198 (HOMO-28); this MO is the bonding combination for overlap of the atomic $3d_{xz}$ orbital on each Cu^{2+} ion with 2p orbitals from each covalently-bound chloride ion.

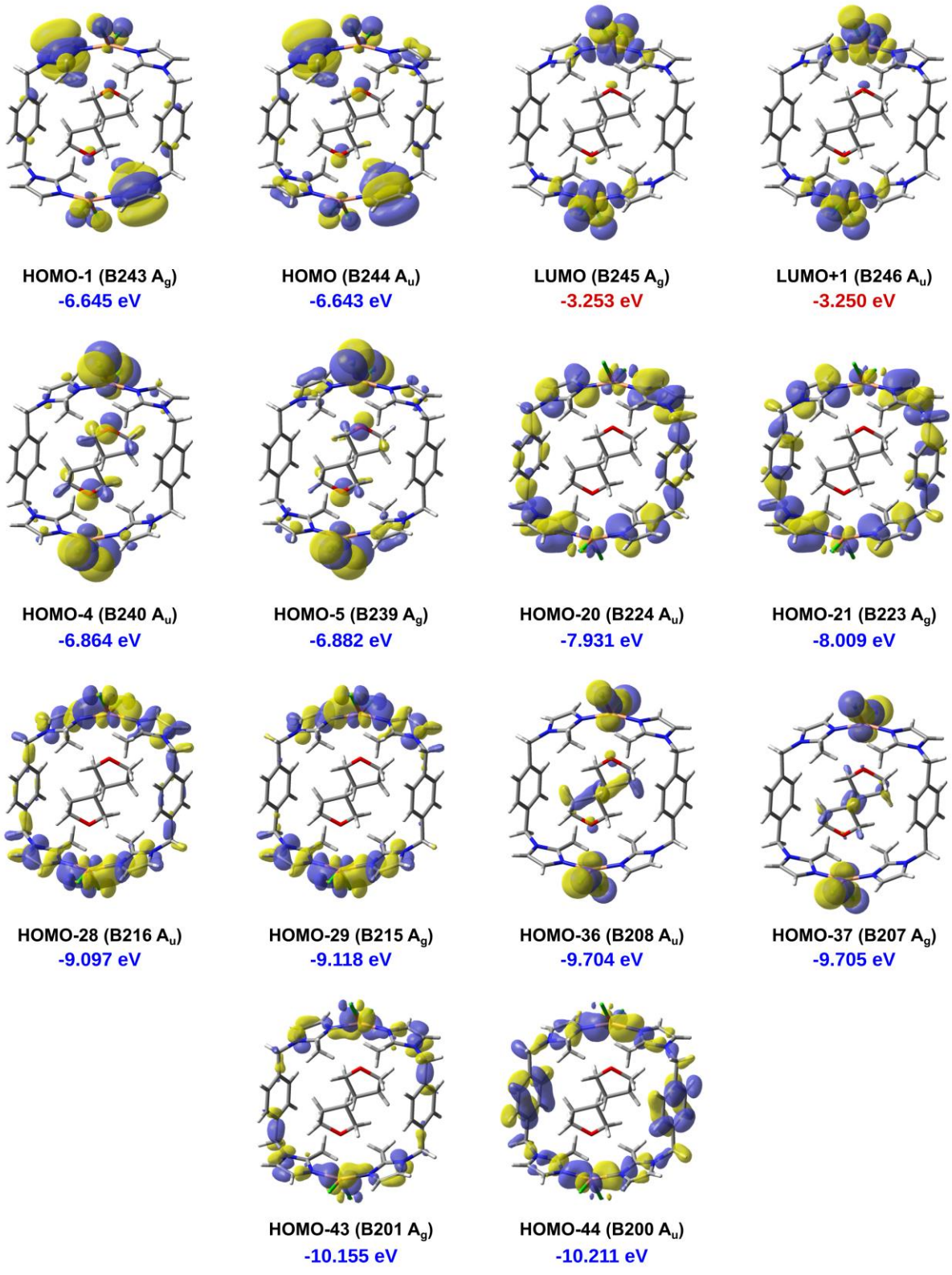

Figure S31: Main molecular orbitals of **4** (Ci symmetry, THF solvent continuum, β-spin) involved in the lowest-energy transitions calculated by TD-DFT and highlighted in **Table S10**. (The HOMO and HOMO-1 are imidazole π orbitals and are not involved in the lowest-energy transitions; they are included for completeness as frontier molecular orbitals of the system.) Symmetry labels are included in parentheses after the MO number.

9. Establishment of the β function

After unsuccessfully attempting to find correlations (**Table S11**) between the energy of the optical transition for the material (ν_{max}), the EPR parameters, and directly measurable structural parameters for the system (e.g., the N–Cu–N bond angle), it became clear that guest-induced perturbation of the host metallocycle would most likely be some function of a combination of empirical parameters such as the van der Waals volume of the guest (its size) as well as the structure of the metallocycle after guest uptake.

The β function described in the main paper, which underpins the bivariate linear correlation of Figure 2, was therefore derived by considering what quantitative structure-based changes might occur upon guest inclusion in the present series of metallocycles. Several possibilities exist: (i) radial stretching/expansion of the metallocycle, (ii) bending of the apices of the metallocycle at the metal centres (which entails deformation of the N–Cu–N bond angles), and (iii) deformation of the Cu–N bond distances in the metallocycle upon stretching of the host to accommodate the guest. We also entertained the crucial idea that the most likely physical response to guest inclusion would be a deformation of the host metallocycle that reflected some combination of the above perturbations.

The parameter β was arrived at as one suitable measure of the guest-induced structural perturbation and is defined as the cage ratio, *R*, multiplied by the van der Waals volume (V_{vdW}) of the guest,

$$\boldsymbol{\beta = R \times V_{vdW}}$$

where *R* = (N–Cu–N bond angle)/(Cu···Cu distance). Importantly, β is based on a combination of variables that describe the geometry of the host and the size of the guest.

The X-ray data relevant to calculation of the β parameter are listed in **Table S12**. In combination with the optical band energy maximum of the materials (ν_{max}) and EPR g-values measuring the tetragonal perturbation of the coordination geometry of the host metallocycle ($g_x - g_y$), the β function was used to discover the bivariate linear correlation plotted in **Figure 2** of the main paper.

Table S11: Correlation matrix (linear) for selected spectroscopic and structural variables listed in Table S12.

		λ_{max}	g_x	g_y	g_z	g_x–g_y	N–Cu–N	ν_{max}	(Cu···Cu)	V_{vdW} (solv.)	Gyration radius
λ_{max}	Pearson Corr.	1	0.05643	-0.97477	-0.6801	0.52563	-0.66288	-0.99859	0.26628	-0.36476	0.06076
λ_{max}	p-value	--	0.91544	9.47E-04	0.13714	0.28417	0.15131	3.00E-06	0.61003	0.47712	0.90898
g_x	Pearson Corr.	0.05643	1	-0.21066	-0.37916	0.87385	-0.73176	-0.04398	0.90943	0.3453	0.50986
g_x	p-value	0.91544	--	0.68868	0.45852	0.02287	0.09828	0.93407	0.01193	0.50263	0.30148
g_y	Pearson Corr.	-0.97477	-0.21066	1	0.72946	-0.65871	0.72015	0.97657	-0.36726	0.16597	-0.27137
g_y	p-value	9.47E-04	0.68868	--	0.09989	0.15484	0.10651	8.17E-04	0.47388	0.75333	0.60293
g_y	Pearson Corr.	-0.6801	-0.37916	0.72946	1	-0.66436	0.58119	0.66408	-0.29784	0.02361	-0.32647
g_y	p-value	0.13714	0.45852	0.09989	--	0.15008	0.22637	0.15031	0.56645	0.9646	0.5277
g_x–g_y	Pearson Corr.	0.52563	0.87385	-0.65871	-0.66436	1	-0.91619	-0.5175	0.87663	0.19748	0.54076
g_x–g_y	p-value	0.28417	0.02287	0.15484	0.15008	--	0.01024	0.29305	0.02189	0.70764	0.26793
N–Cu–N	Pearson Corr.	-0.66288	-0.73176	0.72015	0.58119	-0.91619	1	0.65304	-0.89266	0.15007	-0.22588
N–Cu–N	p-value	0.15131	0.09828	0.10651	0.22637	0.01024	--	0.15969	0.01666	0.77658	0.66694
ν_{max}	Pearson Corr.	-0.99859	-0.04398	0.97657	0.66408	-0.5175	0.65304	1	-0.25825	0.33605	-0.08667
ν_{max}	p-value	3.00E-06	0.93407	8.17E-04	0.15031	0.29305	0.15969	--	0.62124	0.5149	0.87033
(Cu···Cu)	Pearson Corr.	0.26628	0.90943	-0.36726	-0.29784	0.87663	-0.89266	-0.25825	1	0.07789	0.31079
(Cu···Cu)	p-value	0.61003	0.01193	0.47388	0.56645	0.02189	0.01666	0.62124	--	0.8834	0.54883
V_{vdW} (solv.)	Pearson Corr.	-0.36476	0.3453	0.16597	0.02361	0.19748	0.15007	0.33605	0.07789	1	0.89935
V_{vdW} (solv.)	p-value	0.47712	0.50263	0.75333	0.9646	0.70764	0.77658	0.5149	0.8834	--	0.01468
Gyration radius	Pearson Corr.	0.06076	0.50986	-0.27137	-0.32647	0.54076	-0.22588	-0.08667	0.31079	0.89935	1
Gyration radius	p-value	0.90898	0.30148	0.60293	0.5277	0.26793	0.66694	0.87033	0.54883	0.01468	--

Table S12: Experimental and semi-empirical data for 2–6 used for correlation analysis and calculation of the β parameter.

Cpd	Solvate	λ_{max} / nm	ν_{max} / cm^{-1}	g_x	g_y	g_z	g_x–g_y	N–Cu–N / °	(Cu···Cu) / Å	*R*	V_{vdW} / $Å^3$	Gyration radius / Å	β / ° $Å^2$
4	THF	534	18726.59	2.204	2.153	2.101	0.051	156.78	9.921	15.803	77.2	1.3734	1219.992
3	Acetone	581	17211.7	2.2	2.142	2.108	0.058	147.15	10.173	14.465	65.2	1.3488	943.118
6	Pentane	586	17064.85	2.206	2.138	1.988	0.069	149.21	10.001	14.92	95.9	1.9731	1430.828
5	Ether	593	16863.41	2.205	2.136	2.066	0.069	148.26	10.091	14.692	88.4	1.8555	1298.773
2	ACN	619	16155.09	2.197	2.133	1.989	0.064	145.66	9.955	14.632	45.9	1.182	671.6088

10. Video description

The supplementary video attached shows the rapid conversion of **1** to **2**. As the exchange occurs, the crystals turns from green to red in a SC-SC manner. Although cracked the crystal of **2** is sufficiently intact for XRD data collections to be performed

11. References

1. L. Dobrzańska, G. O. Lloyd, C. Esterhuysen and L. J. Barbour. *Angew. Chem. Int. Ed.* 2006, *45*, 5856-5859.
2. MiTeGen. 2016. Online, available: http://www.mitegen.com/ [accessed 28 October 2016].
3. SMART Data Collection Software, Version 5.629; 2003, WI, Bruker AXS Inc., Madison.
4. SADABS, Version 2.05; 2002, WI, Bruker AXS Inc., Madison.
5. G. M. Sheldrick, *Acta Crystallogr. Sect. A: Found. Crystallogr.* 2008, *64*, 112.
6. L. J. Barbour, *J. Supramol. Chem.* 2001, *1*, 189.
7. POV-Ray™, Version 3.6. 2004 Williamstone, Persistence of Vision Raytracer Pty. Ltd.
8. *Cambridge Structural Database and Cambridge Structural Database System, Version 3.55* (February 2015*)*, Cambridge Crystallographic Data Centre, University Chemical Laboratory, Cambridge, England.
9. C. F. Macrae, I. J. Bruno, J. A. Chisholm, P. R. Edgington, P. McCabe, E. Pidcock, L. Rodriguez-Monge, R. Taylor, J. van de Streek and P. A. Wood, *J. Appl. Cryst.* 2008, *41*, 466.
10. C. F. Macrae, P. R. Edgington, P. McCabe, E. Pidcock, G. P. Shields, R. Taylor, M. Towler and J. van de Streek, *J. Appl. Cryst.* 2006, *39*, 453.
11. BIOVA Materials Studio Modeling Environment, Release 2016; Dassault Systèmes: Vélizy-Villacoublay, France, 2015.
12. (a) J. P. Perdew, K. Burke and M. Enzerhof, *Phys. Rev. Lett.* 1997, *78*, 1396; (b) J. P. Perdew, K. Burke and M. Enzerhof, *Phys. Rev. Lett.* 1996, *77*, 3865.
13. S. Grimme, J. Antony, S. Ehrlich and H. Krieg, *J. Chem. Phys.* 2010, *132*, 154104.
14. I. T. Weber and R. W. Harrison, *Protein Eng.* 1999, *12*, 469-474.
15. A. Pedretti, L. Villa and G. Vistoli, *J. Comput.-Aided Mol. Design,* 2004, *18*, 167-173.
16. (a) F. Eisenhaber, P. Lijnzaad, P. Argos, C. Sander and M. Scharf, *J. Comput. Chem.*, 1995, *16*, 273-284. (b) F. Eisenhaber and P. Argos, *J. Comput. Chem.*, 1993, *14*, 1272-1280.
17. M. L. Connolly, *J. Am. Chem. Soc.*, 1985, *107*, 1118-1124.
18. Gaussian 09, Revision E.01: M. J. Frisch, G. W. Trucks, H. B. Schlegel, G. E. Scuseria, M. A. Robb, J. R. Cheeseman, G. Scalmani, V. Barone, B. Mennucci, G. A. Petersson, H. Nakatsuji, M. Caricato, X. Li, H. P. Hratchian, A. F. Izmaylov, J. Bloino, G. Zheng, J. L. Sonnenberg, M. Hada, M. Ehara, K. Toyota, R. Fukuda, J. Hasegawa, M. Ishida, T. Nakajima, Y. Honda, O. Kitao, H. Nakai, T. Vreven, J. A. Montgomery, Jr., J. E. Peralta, F. Ogliaro, M. Bearpark, J. J. Heyd, E. Brothers, K. N. Kudin, V. N. Staroverov, T. Keith, R. Kobayashi, J. Normand, K. Raghavachari, A. Rendell, J. C. Burant, S. S. Iyengar, J. Tomasi, M. Cossi, N. Rega, J. M. Millam, M. Klene, J. E. Knox, J. B. Cross, V. Bakken, C. Adamo, J. Jaramillo, R. Gomperts, R. E. Stratmann, O. Yazyev, A. J. Austin, R. Cammi, C. Pomelli, J. W. Ochterski, R. L. Martin, K. Morokuma, V. G. Zakrzewski, G. A. Voth, P. Salvador, J. J. Dannenberg, S. Dapprich, A. D. Daniels, O. Farkas, J. B. Foresman, J. V. Ortiz, J. Cioslowski, and D. J. Fox, Gaussian, Inc., Wallingford CT, 2013.
19. J. Heyd and G. Scuseria, *J. Chem. Phys.* 2004, *121*, 1187-1192.
20. A. D. McLean and G. S. Chandler, *J. Chem. Phys.* 1980, *72*, 5639-5648.
21. G. Scalmani and M. J. Frisch, *J. Chem. Phys.* 2010, *132*, 114110.
22. GaussSum 3.0: N. M. O'Boyle, A. L. Tenderholt and K. M. Langner. *J. Comp. Chem.* 2008, *29*, 839-845.
23. GaussView, Version 5.0.9: R. Dennington, T. A. Keith and J. M. Millam, Semichem Inc., Shawnee Mission, KS, 2016.